Nano Research

ISSN 1998-0124 CN 11-5974/O4
https://doi.org/10.26599/NR.2026.94909061

Research Article

CuS-based nanoplatform for NIR-II photothermal-enhanced and celastrol-boosted cuproptosis in prostate cancer

Nan Kang[1,§], Zimei Liu[2,§], Fu Tan[1], Haisong Tan[3](✉), Qian Zhang[1](✉)

[1] School of Automation and Intelligent Sensing, Shanghai Jiao Tong University, 800 Dongchuan RD, Shanghai 200240, China

[2] Department of Oncology, Tongren Hospital, Shanghai Jiao Tong University School of Medicine, Shanghai 200050, China

[3] Department of Urology, Shanghai Ninth People's Hospital Affiliated to Shanghai Jiao Tong University School of Medicine, Shanghai 200011, China

[§] Nan Kang and Zimei Liu contributed equally to this work.

Nano Res., **Just Accepted Manuscript** • https://doi.org/10.26599/NR.2026.94909061

https://www.sciopen.com/journal/1998-0124 on Jul. 28, 2026

Just Accepted

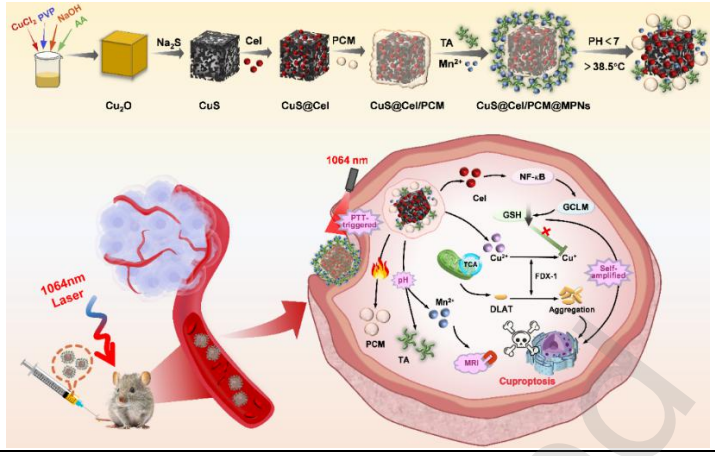

We developed a multifunctional CuS@Cel/PCM-MPNs nanoplatform that combines NIR-II photothermal therapy, acid/thermal-responsive copper and celastrol release, and PA/MR imaging to enhance cuproptosis-based treatment of prostate cancer. This system achieved effective tumor imaging, potent antitumor activity in RM1 tumors, and favorable biosafety, offering a promising theranostic strategy for precise prostate cancer treatment.

Nano Research

Open Access

Research Article

CuS-based nanoplatform for NIR-II photothermal-enhanced and celastrol-boosted cuproptosis in prostate cancer

Nan Kang [1, §], Zimei Liu [2, §], Fu Tan [1], Haisong Tan [3] ✉, and Qian Zhang [1] ✉

[1] *School of Automation and Intelligent Sensing, Shanghai Jiao Tong University, 800 Dongchuan RD, Shanghai 200240, China*
[2] *Department of Oncology, Tongren Hospital, Shanghai Jiao Tong University School of Medicine, Shanghai 200050, P.R. China*
[3] *Department of Urology, Shanghai Ninth People's Hospital Affiliated to Shanghai Jiao Tong University School of Medicine, Shanghai 200011, China*
[§] *Nan Kang and Zimei Liu contributed equally to this work.*

Received: 5 June 2026; **Revised:** 24 July 2026; **Accepted:** 28 July 2026

✉ Address correspondence to Qian Zhang, qianzhang0130@sjtu.edu.cn; Haisong Tan, tanhaisong1983@foxmail.com

Cite this article: *Nano Research*, 2026, 19, 94909061 https://doi.org/10.26599/NR.2026.94909061

ABSTRACT: Cuproptosis-based therapy has emerged as a promising strategy for cancer treatment, but its efficacy is limited by insufficient copper accumulation and poor therapeutic specificity. Herein, we developed a multifunctional CuS@Cel/PCM-MPNs nanoplatform for synergistic prostate cancer theranostics by integrating NIR-II photothermal therapy, responsive drug release, and dual-modal photoacoustic/magnetic resonance imaging. Hollow CuS nanoparticles were used for celastrol (Cel) loading and further modified with phase change material (PCM) and Mn^{2+}-tannic acid metal-polyphenol networks (MPNs). Under acidic and photothermal conditions, the nanosystem enabled responsive release of Cu ions and Cel, leading to amplified oxidative stress and enhanced cuproptosis in tumor cells. Meanwhile, the nanoplatform exhibited excellent photothermal performance under 1064 nm laser irradiation and effective PA/MR imaging capability. Both in vitro and in vivo studies demonstrated efficient tumor accumulation, significant antitumor efficacy against RM1 prostate tumors, and favorable biosafety. Overall, this work provides a promising strategy for synergistic photothermal and cuproptosis-based therapy for precise prostate cancer treatment.

KEYWORDS: hollow CuS nanoparticles, celastrol, photothermal therapy, cuproptosis, prostate cancer, PA/MR imaging

1. Introduction

Prostate cancer is one of the most common malignant tumors in men worldwide and remains a major cause of cancer-related mortality[1-3]. Although conventional therapeutic strategies, including surgery, radiotherapy, chemotherapy, and hormone therapy, have achieved certain clinical benefits, tumor recurrence, therapeutic resistance, and systemic side effects still greatly limit treatment outcomes[4, 5]. Therefore, the development of effective and precise therapeutic strategies for prostate cancer remains highly desirable. Recently, cuproptosis, a newly identified form of copper-dependent regulated cell death, has attracted increasing attention in cancer therapy[6-8]. Distinct from apoptosis, ferroptosis, and necroptosis, cuproptosis is closely associated with mitochondrial metabolism and is characterized by the aggregation of lipoylated proteins induced by intracellular copper overload, ultimately leading to proteotoxic stress and cell death. Because tumor cells generally exhibit elevated metabolic activity and increased sensitivity to oxidative stress, cuproptosis-based therapy provides a promising opportunity for selective tumor eradication. However, the insufficient intracellular accumulation of copper ions and the lack of controllable delivery systems significantly restrict the therapeutic efficacy of cuproptosis[9-11].

Nanoplatforms with stimuli-responsive properties offer an effective approach to overcome these limitations. Among various nanomaterials, copper sulfide nanoparticles have attracted considerable interest owing to their excellent biocompatibility, strong absorption in the second near-infrared (NIR-II) window, and efficient photothermal conversion capability[12-15]. Compared with conventional NIR-I irradiation, NIR-II (especially 1064 nm) offers deeper tissue penetration, reduced photon scattering, and a higher maximum permissible exposure, thereby enabling more efficient and safer photothermal treatment of deep-seated tumors. Under NIR-II laser irradiation, CuS can efficiently generate localized hyperthermia, which not only directly damages tumor tissues but also promotes drug release and accelerates copper ion liberation. Recent studies have further demonstrated that CuS-based nanoplatforms can achieve efficient tumor ablation through NIR-triggered photothermal therapy while serving as multifunctional carriers for combination therapeutic strategies, highlighting their considerable potential for cancer theranostics[16]. Moreover, hollow CuS nanostructures possess large internal cavities and high surface areas, making them suitable carriers for therapeutic agents[17-18]. Celastrol (Cel), a

natural bioactive compound with pro-oxidative and anticancer activities, has been reported to disrupt intracellular redox homeostasis and enhance oxidative stress in tumor cells[19-22]. Therefore, the combination of CuS-mediated cuproptosis and Cel-induced oxidative stress may provide synergistic therapeutic effects against tumors[23-26]. In addition, the tumor microenvironment is generally characterized by weak acidity and elevated oxidative stress, which can be exploited to design responsive nanosystems for precise drug release. Phase change materials (PCM) can effectively prevent premature drug leakage and achieve thermally triggered release under photothermal heating[27-30], while metal-polyphenol networks (MPNs) exhibit good biocompatibility and pH-responsive degradation behavior[31-34]. Furthermore, the incorporation of Mn^{2+} into MPNs can endow nanosystems with magnetic resonance (MR) imaging capability, enabling imaging-guided therapy[35, 36]. Meanwhile, the strong NIR absorption of CuS also makes it suitable for photoacoustic (PA) imaging, allowing dual-modal imaging for improved tumor diagnosis and therapeutic monitoring[37-40].

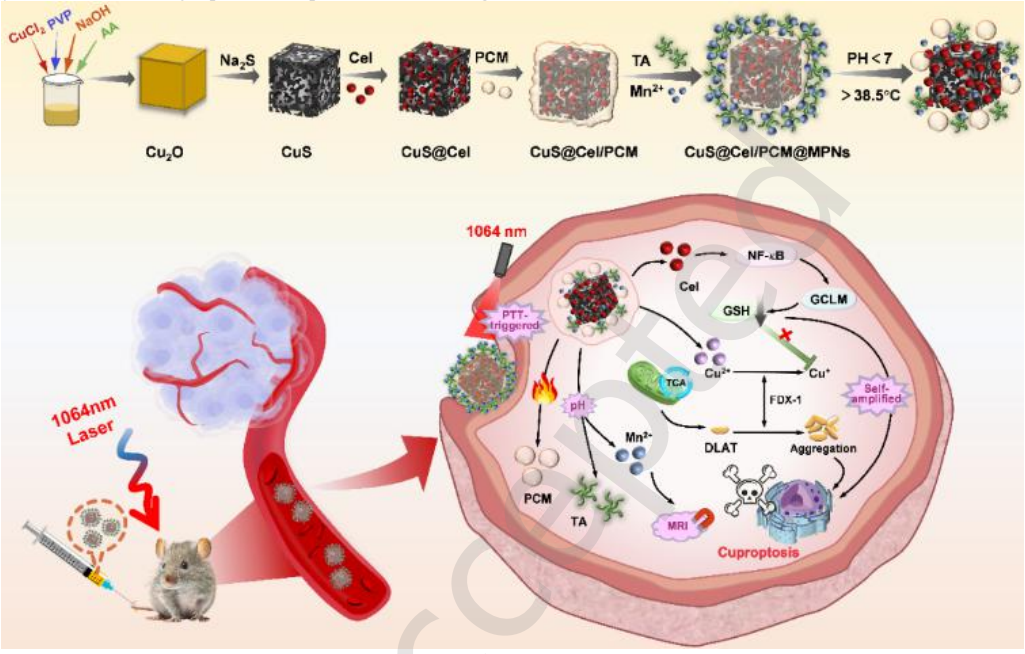

Scheme 1. Schematic illustration of the synthesis of CuS@Cel/PCM-MPNs and their application in NIR-II-triggered, pH/thermal-responsive drug release and cuproptosis-based synergistic therapy for prostate cancer.

Herein, we developed a multifunctional CuS@Cel/PCM-MPNs nanoplatform for synergistic prostate cancer theranostics. As illustrated in **Scheme 1**, Hollow CuS nanoparticles were first synthesized as carriers for Cel loading, followed by encapsulation with PCM(1-tetradecanol) and coating with Mn^{2+}-tannic acid MPNs. The obtained nanosystem exhibited excellent NIR-II photothermal performance, pH-/thermal-responsive release behavior, and enhanced catalytic activity under tumor-mimicking conditions. More importantly, responsive release of Cu ions and Cel effectively disrupted intracellular redox homeostasis and mitochondrial function, thereby amplifying cuproptosis in tumor cells. In addition, the nanosystem enabled effective PA/MR dual-modal imaging and demonstrated significant antitumor efficacy with favorable biosafety in RM1 prostate tumor models. This work provides a promising strategy for integrating photothermal therapy and cuproptosis-based therapy for precise prostate cancer treatment.

2. Results and Discussion

2.1 Preparation and Characterization

Cu_2O nanoparticles were first synthesized and served as sacrificial templates for constructing hollow nanostructures[10]. As shown in **Figure 1a**, transmission electron microscopy (TEM) images revealed that the obtained Cu_2O nanoparticles exhibited a uniform cubic morphology with an average size of approximately 100 nm and smooth surfaces. High-resolution TEM (HRTEM) images displayed clear lattice fringes with an interplanar spacing of 0.245 nm, corresponding to the (111) plane of Cu_2O, indicating good crystallinity. Energy-dispersive spectroscopy (EDS) mapping further demonstrated a homogeneous distribution of Cu and O elements, confirming the high purity of the nanoparticles. Subsequently, CuS nanostructures were obtained via a sulfuration process based on the Kirkendall effect[14]. As shown in **Figure 1b**, the morphology evolved from solid cubes to hollow and porous structures, with reduced interior contrast and roughened edges, indicative of void formation. The HRTEM image showed a lattice spacing of 0.329 nm, corresponding to the (100) plane of CuS, confirming successful phase transformation. EDS mapping revealed uniform distribution of Cu and S elements throughout the nanoparticles. The formation of hollow structures is beneficial for drug loading due to the increased internal cavity and surface area. Cel was then loaded into the hollow CuS, followed by encapsulation with a PCM and further coating with a MPNs to obtain the final CuS@Cel/PCM-MPNs nanoplatform. As shown in **Figure 1c**, the overall morphology was well maintained after multistep modification, while a relatively blurred and low-contrast outer layer appeared compared to bare CuS, which could be attributed to the PCM coating[29]. Moreover, EDS mapping showed that Mn was mainly distributed on the

outer region, whereas Cu and S remained uniformly distributed in the core, confirming the successful formation of a core-shell structure with an outer Mn^{2+}-TA layer. This hierarchical structure enables the integration of drug loading, thermal responsiveness, and environmental responsiveness.

The crystalline structures were characterized by X-ray diffraction (XRD) **(Figure 1d, 1g)**. The diffraction peaks of Cu_2O were consistent with the standard pattern (PDF#05-0667), with no detectable impurity peaks. After sulfuration, the peaks matched well with standard CuS (PDF#06-0464), indicating complete phase transformation. X-ray photoelectron spectroscopy (XPS) was employed to analyze the surface composition and valence states. For Cu_2O **(Figure 1e, f)**, the Cu 2p spectrum exhibited two characteristic peaks at approximately 932.4 eV (Cu $2p^{3/2}$) and 952.2 eV (Cu $2p^{1/2}$), which are typical of Cu^+ species, without obvious satellite peaks. The O 1s spectrum showed a main peak at ~530.1 eV, corresponding to lattice oxygen. After conversion to CuS **(Figure 1h,1i)**, the Cu 2p spectrum displayed peaks at ~932.6 and ~952.5 eV along with weak satellite features, indicating the coexistence of Cu^+ and Cu^{2+}. The S 2p spectrum could be deconvoluted into peaks at ~161.8 and ~163.0 eV, corresponding to S^{2-} species[10]. These results confirm the successful transformation from Cu_2O to CuS.

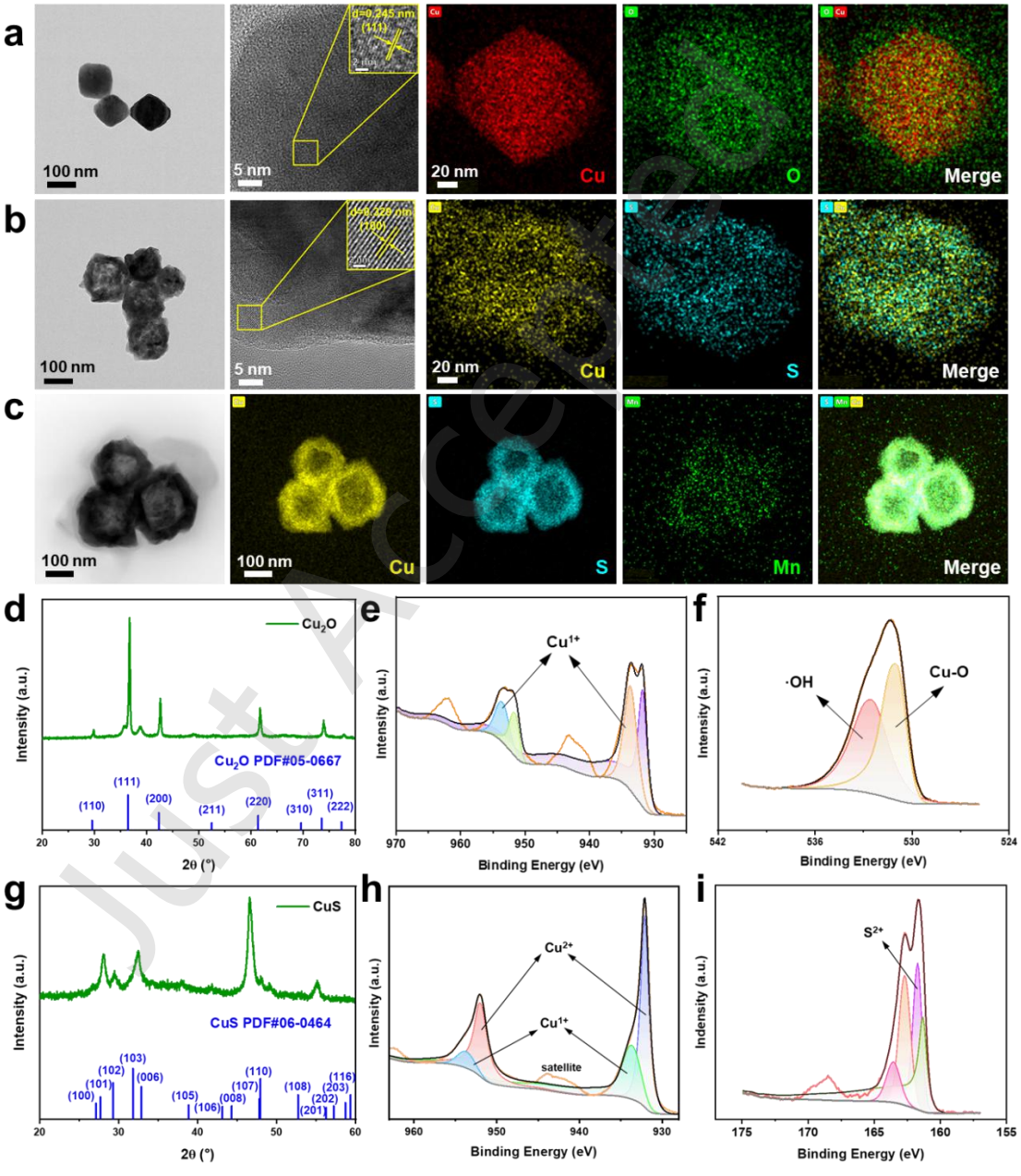

Figure 1. Preparation and characterization of CuS@Cel/PCM-MPNs nanoplatform. (a) TEM, HRTEM images and EDS mapping of Cu_2O. (b) TEM, HRTEM images and EDS mapping of CuS. (c) TEM image and EDS mapping of CuS@Cel/PCM-MPNs. (d) XRD patterns of Cu_2O. (e, f) XPS spectra of Cu_2O. (g) XRD patterns of CuS. (h, i) XPS spectra of CuS.

2.2 In vitro Photothermal Performance and Catalytic/Responsive Release

As shown in **Figure 2a**, the UV-vis-NIR absorption spectrum of CuS exhibits a broad absorption band in the NIR-II region, indicating its excellent photothermal properties[15]. Moreover, the absorption intensity of CuS

increases with increasing concentration, demonstrating a clear concentration-dependent behavior (**Figure S1**). Subsequently, based on the standard calibration curve of Cel, its characteristic absorption peak was determined to be located at approximately 422 nm (**Figure S2**). The UV-vis-NIR spectra of the stepwise synthesized products reveal that, after drug loading, a distinct characteristic absorption peak of Cel appears compared with bare CuS, confirming the successful loading of Cel. The encapsulation efficiency was calculated to be 78.94%. In addition, these spectral changes indirectly verify the effective encapsulation of the PCM and the successful modification with MPNs. Dynamic light scattering (DLS) analysis **(Figure 2b)** showed a gradual increase in hydrodynamic size from ~110 nm (CuS) to ~160-170 nm after PCM and MPNs coating, consistent with stepwise surface modification. Meanwhile, the zeta potential became more negative after MPNs coating, which could be attributed to the phenolic hydroxyl groups of tannic acid, suggesting improved colloidal stability in aqueous environments[17]. To further evaluate the physiological stability of CuS@Cel/PCM-MPNs, the nanoparticles were incubated in complete cell culture medium containing 10% FBS, and their hydrodynamic diameters were monitored over 48 h by DLS. As shown in Figure 2c, no obvious change in particle size was observed during the incubation period (0–48 h), indicating excellent colloidal stability under physiologically relevant conditions. This favorable stability is beneficial for maintaining nanoparticle integrity during circulation and subsequent biological applications **(Figure 2c).** Collectively, these results demonstrate the successful construction of the CuS@Cel/PCM- MPNs nanoplatform with well-defined structure and surface properties.

The photothermal performance of CuS@Cel/PCM-MPNs nanoplatform under 1064 nm laser irradiation was systematically investigated. As shown in **Figure 2d**, the temperature of the nanoparticle dispersion increased rapidly with increasing concentration, exhibiting a clear concentration-dependent photothermal effect. Specifically, higher concentrations resulted in faster heating rates and higher equilibrium temperatures, indicating efficient light-to-heat conversion capability. This enhanced photothermal behavior is primarily attributed to the intrinsic NIR absorption of CuS. Notably, the use of a 1064 nm laser within the NIR-II window is advantageous because of its deeper tissue penetration and reduced optical scattering compared with conventional NIR-I irradiation. These characteristics facilitate more efficient heat deposition in tumor tissues and improve the potential for treating deeply located tumors, further supporting the rationale for employing NIR-II photothermal therapy in this study. Subsequently, the influence of laser power density on the photothermal performance was examined. As illustrated in **Figure 2e**, the temperature elevation increased progressively with increasing laser power, suggesting that the photothermal effect can be effectively regulated by external irradiation conditions. Notably, similar concentration- and power-dependent trends were also observed for bare CuS nanoparticles **(Figure S3)**, confirming that CuS acts as the dominant photothermal agent within the nanoplatform. Furthermore, the photothermal stability of CuS@Cel/PCM-MPNs nanoplatform was evaluated through repeated laser on/off irradiation cycles. As shown in **Figure 2f**, negligible attenuation in temperature rise was observed over four consecutive cycles, demonstrating excellent photothermal stability and reproducibility. Consistently, infrared thermal imaging **(Figure 2g)** revealed a uniform and rapid temperature increase under laser irradiation, highlighting the potential of this system for precise and controllable thermal modulation.

To further elucidate the functional mechanism of the nanoplatform beyond photothermal effects, its stimuli-responsive release behavior and catalytic activity were systematically investigated[10, 11]. As shown in **Figure 2h**, the release of Cu ions was quantified by inductively coupled plasma mass spectrometry (ICP-MS) under different conditions. Under neutral conditions, only a limited amount of Cu ions was released, whereas a markedly enhanced release was observed in acidic environments, increasing to ~100 μg mL^{-1}. This pH-dependent behavior can be attributed to the decomposition of the MPNs metal-polyphenol network under acidic conditions, which exposes and partially degrades the CuS core. Notably, the released Cu ions may further induce copper-dependent cytotoxicity, including cuproptosis, thereby providing an additional therapeutic pathway[24]. The release behavior of Cel was further evaluated **(Figure 2i)**. At room temperature and under neutral conditions, only ~10% of Cel was released within 7 h, indicating that the outer coating effectively inhibited premature drug leakage. In contrast, under 1064 nm laser irradiation and acidic conditions, when the temperature increased above 38.5 °C, the release of Cel was markedly accelerated due to the melting of the PCM and the dissociation of the MPNs, reaching approximately 50% within 7 h. The results showed that Cel release was significantly accelerated under external stimuli, indicating that the PCM layer and MPNs coating could effectively regulate drug release in a controlled manner.

The catalytic activity of the nanoplatform was then assessed using 3,3′,5,5′-tetramethylbenzidine (TMB) as a substrate[10]. The characteristic absorption peak of TMB at 650 nm was confirmed by time-dependent UV–vis spectra **(Figure S4)**, and the absorbance at this wavelength was used for quantitative analysis. The nanoplatform exhibited enhanced catalytic oxidation of TMB under acidic and high-temperature conditions, as evidenced by a pronounced increase in absorbance at 650 nm **(Figure 2j)**. Compared with neutral conditions (25 °C, pH 7.4), both acidic pH (5.0) and elevated temperature (55 °C) significantly promoted TMB oxidation, with the highest activity observed under combined acidic and thermal conditions. Kinetic analysis further confirmed this trend **(Figure 2k)**. At room temperature, catalytic activity increased with decreasing pH, indicating that acidic conditions facilitate Cu ion release from the nanoplatform and thereby enhance catalytic efficiency. Similarly, H_2O_2 concentration-dependent experiments **(Figure 2l)** demonstrated that higher substrate levels led to faster and stronger oxidation responses, confirming its role as a key reactant in the catalytic process. In addition, the transmission electron microscopy images further illustrate the degradation of the CuS@Cel/PCM-

MPNs nanoplatform under acidic conditions and at high temperatures induced by laser irradiation, leading to the release of copper ions and Cel **(Figure S5)**. Overall, the catalytic performance is jointly regulated by pH, temperature, and H_2O_2 concentration. The enhanced activity under acidic and oxidative environments is attributed to accelerated Cu ion release and increased substrate reactivity, which synergistically promote the catalytic process.

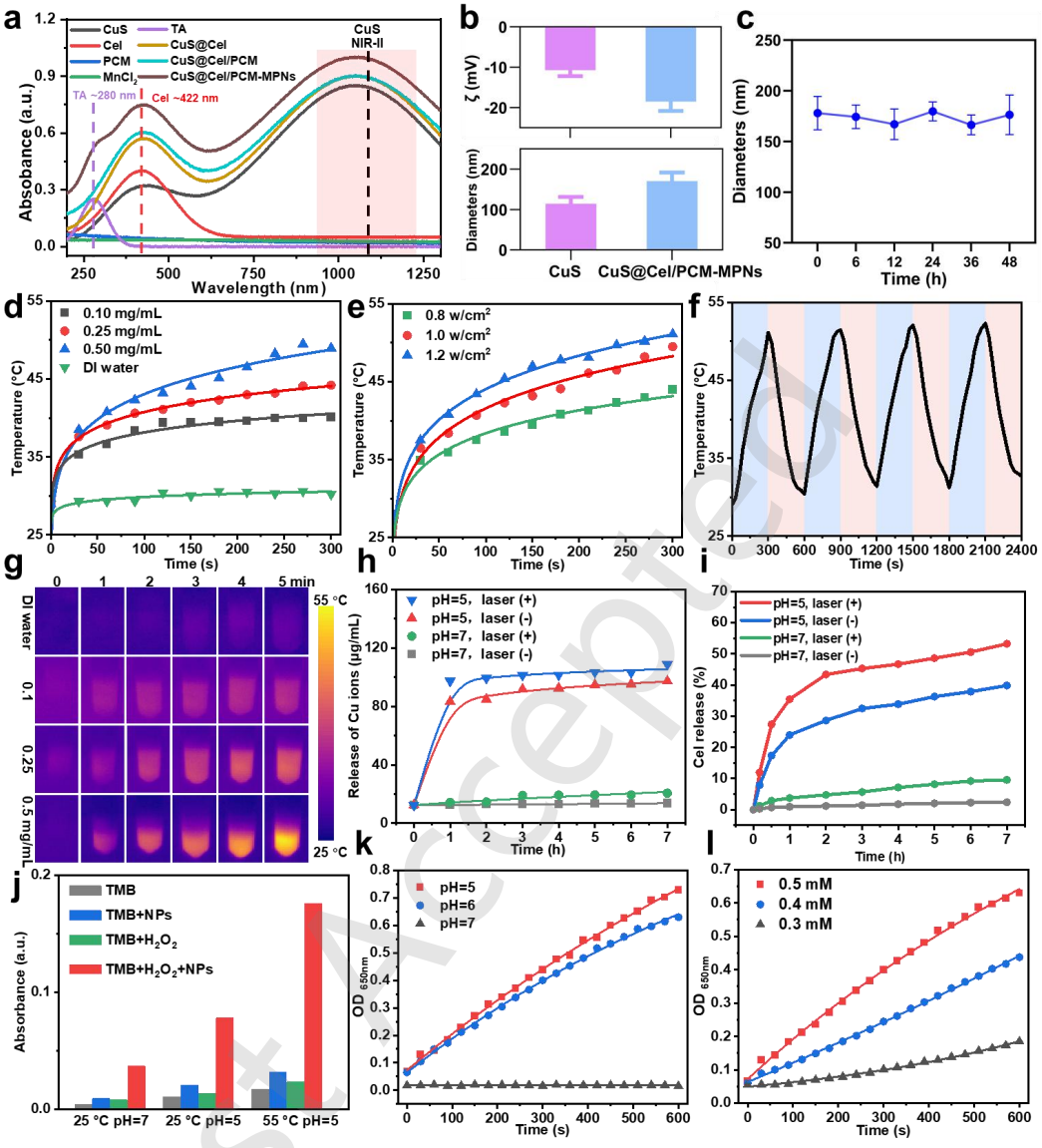

Figure 2. Photothermal performance and catalytic/responsive release of CuS@Cel/PCM-MPNs nanoplatform. (a) UV-vis-NIR absorption spectra of stepwise assembled nanoplatforms. (b) DLS values and ζ-potential values of CuS and CuS@Cel/PCM-MPNs. (c) Hydrodynamic size stability of CuS@Cel/PCM-MPNs dispersed in complete cell culture medium containing 10% FBS over 48 h. (d) Temperature elevation curves of CuS@Cel/PCM-MnTA at different concentrations under 1064 nm laser irradiation. (e) Temperature elevation under different laser power densities. (f) Photothermal stability over four on/off irradiation cycles. (g) Infrared thermal images during laser irradiation. (h) Cu ion release measured by ICP-MS under different conditions. (i) Release profiles of Cel under different conditions. (j) Absorbance intensity of oxidized TMB at 650 nm under different conditions. (k, l) Time-dependent absorbance changes of TMB at 650 nm under different conditions.

2.3 Cell uptake and cytotoxicity

The cellular uptake behavior of the Cy5.5-labeled CuS@Cel/PCM-MPNs nanoplatform was evaluated in RM1 cells using confocal laser scanning microscopy (CLSM)[24]. As shown in **Figure 3a**, a progressive increase in intracellular fluorescence was observed from 0 to 5 h, indicating efficient and time-dependent internalization of the nanosystems. The strongest signal at 5 h further confirmed enhanced cellular accumulation over time. This efficient uptake may be attributed to the nanoscale size and the presence of a phase-change material–based metal–polyphenol network shell, which can facilitate cellular interaction and endocytic internalization without significantly hindering membrane transport. In addition, such surface architecture may also contribute to improved tumor affinity[32, 34]. Colocalization analysis suggested that the internalized nanosystems were mainly involved in endo-lysosomal trafficking, as partial overlap between Cy5.5 fluorescence and lysosomal compartments was observed at all time points (**Figure 3b**). To further assess intratumoral transport behavior, a 3D tumor spheroid model was employed to better simulate the solid tumor microenvironment[17, 41]. Compared with conventional two-dimensional (2D) cell cultures, 3D tumor spheroids more faithfully recapitulate the complex architecture of solid

tumors, including enhanced cell-cell and cell-matrix interactions, diffusion barriers, and gradients of oxygen and nutrients. Therefore, they provide a more physiologically relevant model for evaluating nanoparticle penetration, cellular uptake, and therapeutic efficacy before in vivo studies. As shown in **Figure 3c**, the CuS@Cel/PCM-MPNs nanoplatform exhibited efficient penetration into tumor spheroids rather than being restricted to the peripheral region. Cross-sectional CLSM imaging at different depths revealed detectable fluorescence throughout the spheroid structure, with relatively higher intensity in the central region (~30 μm). In addition, overall fluorescence intensity increased gradually from 1 to 5 h, indicating time-dependent penetration and accumulation within the spheroids. Collectively, these results demonstrate efficient cellular internalization and favorable tumor-penetrating capability of the nanosystems. The successful penetration throughout the 3D tumor spheroids further suggests that the nanoplatform can effectively overcome diffusion barriers within tumor-like tissues, highlighting its potential for improved intratumoral delivery under physiologically relevant conditions.

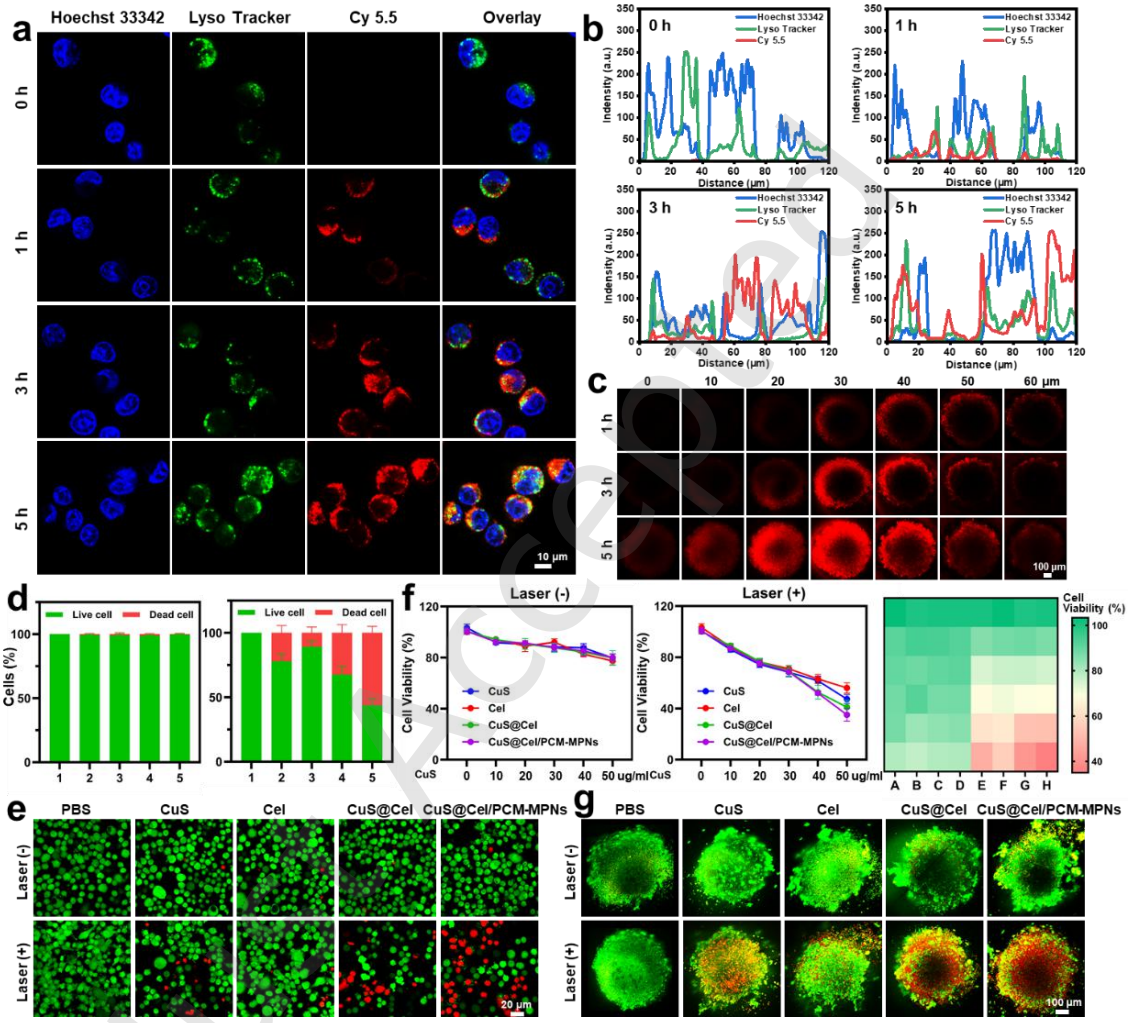

Figure 3. Cell uptake and cytotoxicity. (a, b) CLSM images and colocalization analysis of RM1 cells interacted with CuS@Cel/PCM-MPNs nanoplatform at different time points (0, 1, 3, and 5 h). Cell nuclei were counterstained with Hoechst 33342 (blue), and lysosomes were labeled with Lyso Tracker (green). Cy5.5 fluorescence (red) represents the distribution of the CuS@Cel/PCM-MPNs nanoplatform. (c) CLSM images showing the penetration behavior of Cy5.5-labeled CuS@Cel/PCM-MPNs in RM1 tumor spheroids. Cross-sectional images were obtained at different depths (0–60 μm) to evaluate intratumoral distribution. (d, e) Representative CLSM images of RM1 cells stained with Calcein-AM (live cells, green) and PI (dead cells, red) after various treatments, with corresponding quantitative analysis of cell populations. (f) Summary of cell viabilities presented as line charts and a corresponding heatmap visualization of the concentration-dependent survival rates (Group A: CuS, B: Cel, C: CuS@Cel, D: CuS@Cel/PCM-MPNs, E: CuS+Laser, F: Cel+Laser, G: CuS@Cel+Laser, H: CuS@Cel/PCM-MPNs+Laser). (g) Representative CLSM images of 3D RM1 tumor spheroid stained with Calcein-AM/PI after different treatments in the presence or absence of 1064 nm laser irradiation.

Prior to evaluating the therapeutic efficacy, the biocompatibility of CuS, Cel, CuS@Cel, and CuS@Cel/PCM-MPNs was systematically investigated. To visually confirm the mode of cell death, RM1 cells were co-stained with Calcein-AM and Propidium Iodide (PI) for live/dead cell imaging **(Figure 3d, 3e)**. In the absence of laser irradiation, almost all cells across the PBS and four material groups exhibited intense green fluorescence, indicating high viability. This was further supported by the quantitative statistical analysis. However, upon 1064 nm laser irradiation, a significant increase in red fluorescence (dead cells) was observed in the CuS@Cel/PCM-MPNs treated group, confirming the potent phototoxicity of the final nanosystem. Subsequently, RM1 cells were incubated with various concentrations of these materials in the absence of laser irradiation. As shown in **Figure S6**, the CCK-8 assay results

revealed that even at their respective maximum concentrations, the cell viability remained above 80%. These results indicate that all the building blocks and the final integrated nanosystem possess excellent biocompatibility and negligible dark toxicity, providing a safe foundation for further biomedical applications. Subsequently, the in vitro phototherapeutic effect was evaluated under 1064 nm laser irradiation. In contrast to the dark groups, all groups showed a concentration-dependent decrease in cell viability upon laser exposure. Notably, the CuS@Cel/PCM-MPNs group exhibited the most significant killing effect, with cell viability plummeting to approximately 30% at the highest concentration. To provide a more intuitive comparison, line charts and a heatmap were utilized to visualize the survival trends **(Figure 3f)**. The line charts clearly distinguish the minimal impact of materials alone (Laser -) versus the potent inhibitory effect of the combined treatments (Laser +). The heatmap further corroborates this, where the transition from green (high viability) to red (low viability) in the bottom-right corner highlights that the CuS@Cel/PCM-MPNs (Laser +) group achieved the highest therapeutic efficacy, with a survival rate below 40%. To further simulate the complex tumor microenvironment, RM1-derived 3D tumor spheroid were employed for cytotoxicity evaluation[24]. As shown in **Figure 3g**, consistent with the 2D cell results, the 3D tumor spheroid treated with CuS@Cel/PCM-MPNs and laser irradiation showed extensive red fluorescence throughout the spheroid, while the no-laser groups remained predominantly green. These results collectively demonstrate that the CuS@Cel/PCM-MPNs nanosystem, combined with NIR-II laser irradiation, exerts a robust and superior antitumor effect in both 2D and 3D models.

2.4 Synergistic Mechanism of CuS@Cel/PCM-MPNs for Amplified Cuproptosis

To elucidate the therapeutic mechanism of CuS@Cel/PCM-MPNs, we focused on copper-dependent cell death (cuproptosis), a mitochondria-associated process driven by intracellular copper overload and subsequent proteotoxic stress[7, 9, 42]. As illustrated in **Figure 4a**, CuS@Cel/PCM-MPNs initiate a cascade of intracellular events centered on copper accumulation and redox imbalance. In this system, CuS serves as the primary copper source to trigger cuproptosis, while Cel functions as an adjuvant to reinforce this process by aggravating intracellular stress responses. Copper accumulation is the initiating event. Since intracellular copper overload is the prerequisite for cuproptosis initiation, the markedly elevated intracellular Cu level provides the fundamental basis for the subsequent copper-dependent cellular events observed in this study.

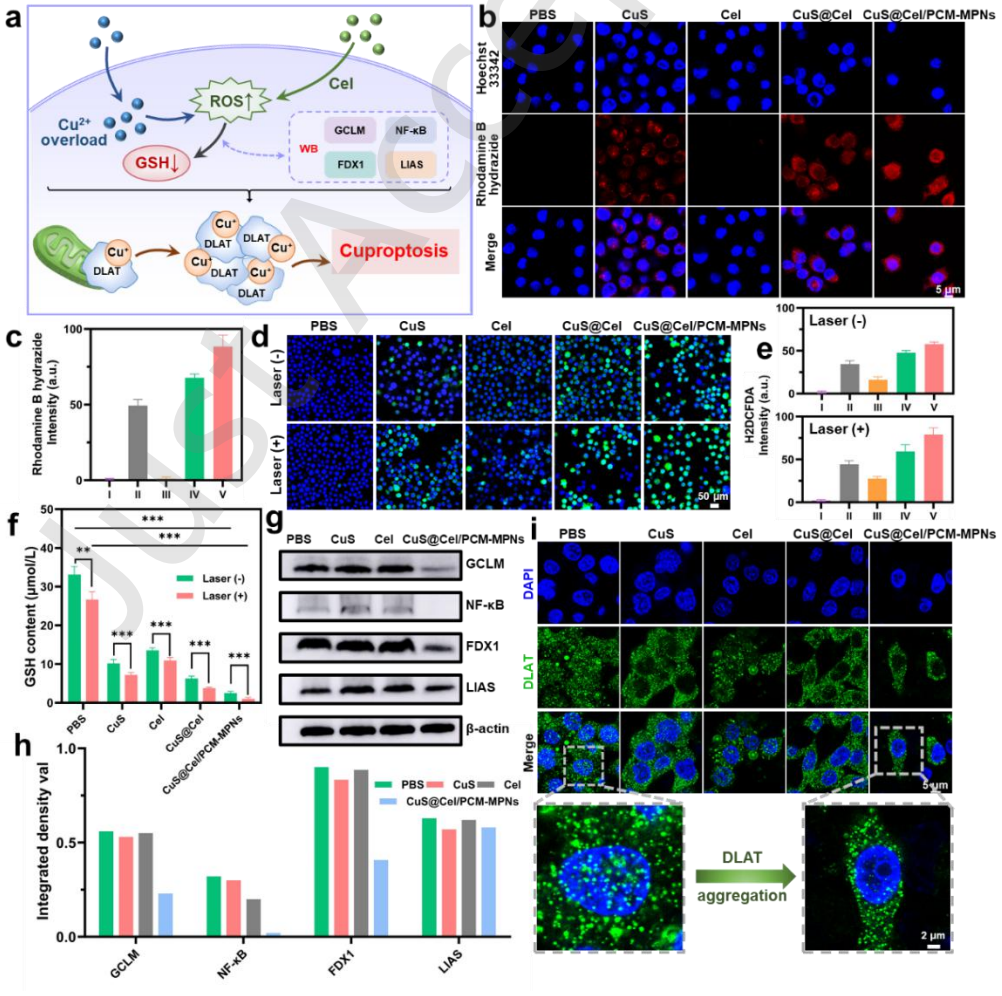

Figure 4. Mechanistic investigation of synergistic cuproptosis induction in RM1 cells. (a) Schematic showing the biological mechanism of cuprotosis. (b, c) CLSM images of intracellular copper ions detected by Rhodamine B, with corresponding quantitative analysis. (d, e) CLSM images showing

intracellular ROS generation, with corresponding quantitative analysis. (f) Quantitative analysis of intracellular GSH levels. (g, h) Western blot analysis of key cuproptosis-related proteins, with corresponding quantitative analysis. (i) CLSM images showing the distribution of DLAT.

As shown in **Figure 4b and 4c**, CuS-based treatments significantly elevated intracellular copper levels, which was further enhanced under laser irradiation due to accelerated Cu release. Notably, the enhanced intracellular copper accumulation in the presence of Cel suggests that Cel contributes to increasing the intracellular copper burden, thereby facilitating copper-dependent cytotoxicity[19, 22-24]. Subsequently, intracellular redox homeostasis is severely disrupted. Reactive oxygen species(ROS) levels were markedly increased after treatment, especially in the CuS@Cel/PCM-MPNs group **(Figure 4d, 4e)**. This is attributed not only to Cu-mediated catalytic ROS generation, but also to the intrinsic pro-oxidative activity of Cel, which further amplifies oxidative stress. Correspondingly, Glutathione(GSH) levels were significantly depleted, indicating impaired antioxidant defense **(Figure 4f)**. Meanwhile, Cel-induced disruption of redox homeostasis further sensitized tumor cells to copper-induced stress, resulting in amplified oxidative damage. The simultaneous ROS accumulation and GSH depletion further weaken intracellular copper-buffering capacity and amplify copper-mediated oxidative stress, thereby creating a cellular environment favorable for the progression of cuproptosis.

At the molecular level, Western blot analysis revealed a coordinated suppression of cellular defense systems **(Figure 4g)**. Compared with PBS, CuS or Cel alone induced minimal changes, whereas the combined treatment caused more pronounced effects. Specifically, NF-κB was significantly inhibited and GCLM was markedly downregulated, indicating impaired GSH synthesis and weakened antioxidant capacity. Meanwhile, FDX1 expression decreased, suggesting disrupted mitochondrial electron transfer and copper handling under copper overload. In contrast, LIAS showed only slight changes, implying that the lipoylation machinery remained largely intact. This imbalance promotes the binding of copper to proteins such as DLAT, thereby exacerbating their aggregation and mitochondrial dysfunction, ultimately inducing cuproptosis[24]. **Figure 4h** shows the results of the quantitative analysis of the WB. Consistently, CLSM demonstrated that DLAT underwent a transition from a diffuse distribution to pronounced aggregation after treatment **(Figure 4i)**, providing direct evidence of copper-dependent protein aggregation. Importantly, these molecular changes are highly consistent with the characteristic events of cuproptosis. Specifically, intracellular copper overload is accompanied by dysregulation of FDX1-mediated mitochondrial metabolism and aggregation of the lipoylated TCA-cycle protein DLAT, which together constitute representative molecular features of copper-dependent cell death. Therefore, the coordinated alterations in these key proteins, together with the observed DLAT aggregation, provide direct molecular evidence supporting the activation of cuproptosis rather than relying on a single biomarker. Among them, Cel acts as a synergistic amplifier by both promoting intracellular copper accumulation and enhancing cellular susceptibility to copper-induced stress, ultimately facilitating CuS-triggered cuproptosis.

2.5 RNA Sequencing and Analysis

To explore the molecular mechanism underlying CuS@Cel treatment, RNA sequencing was performed to analyze transcriptional changes in tumor cells[21, 23]. The Venn diagram represents the overlap of differentially expressed genes among different treatment comparisons. As shown in the **Figure 5a**, a total of 402 genes were commonly regulated among groups, while 516, 154, and 1255 genes were uniquely distributed, indicating both shared and treatment-specific transcriptional responses. Subsequently, The volcano plot **(Figure 5b)** reveales extensive changes in gene expression in the CuS@Cel/PCM-MPNs and PBS groups, with 3470 genes upregulated and 2984 genes downregulated compared with the control group, indicating that the treatment group induced significant transcriptional reprogramming. Further kyoto encyclopedia of genes and genomes (KEGG) enrichment analysis revealed distinct pathway alterations between different treatments **(Figure 5c, d)**. In the Cel-treated group, the differentially expressed genes were mainly enriched in cell cycle, NF-kappa B signaling pathway, Glutathione metabolism, and oxidative stress-related processes, indicating that Cel primarily regulates cell proliferation and intracellular redox balance. In contrast, the CuS-treated group showed enrichment in cell cycle, Protein processing in endoplasmic reticulum, Glutathione metabolism, and Citrate cycle (TCA cycle), suggesting the involvement of protein homeostasis and mitochondrial metabolism in CuS-induced cellular responses. Meanwhile, the enrichment of protein processing-related pathways also reflects the cellular stress response induced by photothermal effects. Notably, overlapping pathways such as glutathione metabolism and cell cycle were observed in both groups, indicating a potential synergistic effect.

The heatmap **(Figure 5e)** reflected the integrated effect of CuS@Cel, where genes involved in cuproptosis, including Fdx1, Lias, Lipt1, and Dlat, were generally downregulated, indicating dysregulation of mitochondrial metabolic activity. In contrast, oxidative stress-related genes such as Slc7a11, Gclc, and Nqo1 were upregulated, indicating activation of the glutathione-dependent antioxidant system in response to elevated oxidative stress. Meanwhile, heat shock genes, including Hspa1a and Hspa5, were markedly upregulated, confirming the activation of photothermal stress responses. These coordinated changes highlight the synergistic regulation of mitochondrial metabolism, redox balance, and thermal stress in the combined system. The Gene Ontology (GO) chord diagram **(Figure 5f)** revealed that differentially expressed genes were mainly associated with metal ion binding, mitochondrial function, and stress-related processes such as DNA damage, apoptosis, and cell cycle regulation, while also highlighting their tight interconnection across these pathways. Consistently, protein-protein interaction analysis **(Figure 5g)** revealed several highly connected functional modules, including cuproptosis and mitochondrial metabolism (e.g., Dlat, Pdha1), oxidative stress regulation (e.g., Slc7a11, Gclc), and protein homeostasis/proteasome components. Notably, hub proteins such as Myc, Hspa5, and Hsp90aa1 were located at

the intersection of these modules, suggesting a bridging role that links metabolic disruption, stress response, and protein regulation. Finally, gene set enrichment analysis (GSEA) **(Figure 5h)** provided further support for these alterations, showing a suppression of the NF-kappa B signaling pathway, accompanied by an activation of Citrate cycle (TCA cycle) and Glutathione metabolism[7].

Importantly, these transcriptomic alterations are highly consistent with the experimental observations at the cellular and protein levels, demonstrating coordinated regulation of copper metabolism, mitochondrial function, protein homeostasis, and oxidative stress. This integrated molecular signature further supports that cuproptosis is a major mechanism underlying the therapeutic effects of CuS@Cel/PCM-MPNs.

Taken together, the sequential evidence obtained from intracellular copper accumulation, redox imbalance, coordinated regulation of cuproptosis-associated proteins, DLAT aggregation, and transcriptomic analyses consistently delineates the progression from copper overload to cuproptosis, forming a coherent mechanistic framework for the therapeutic action of CuS@Cel/PCM-MPNs.

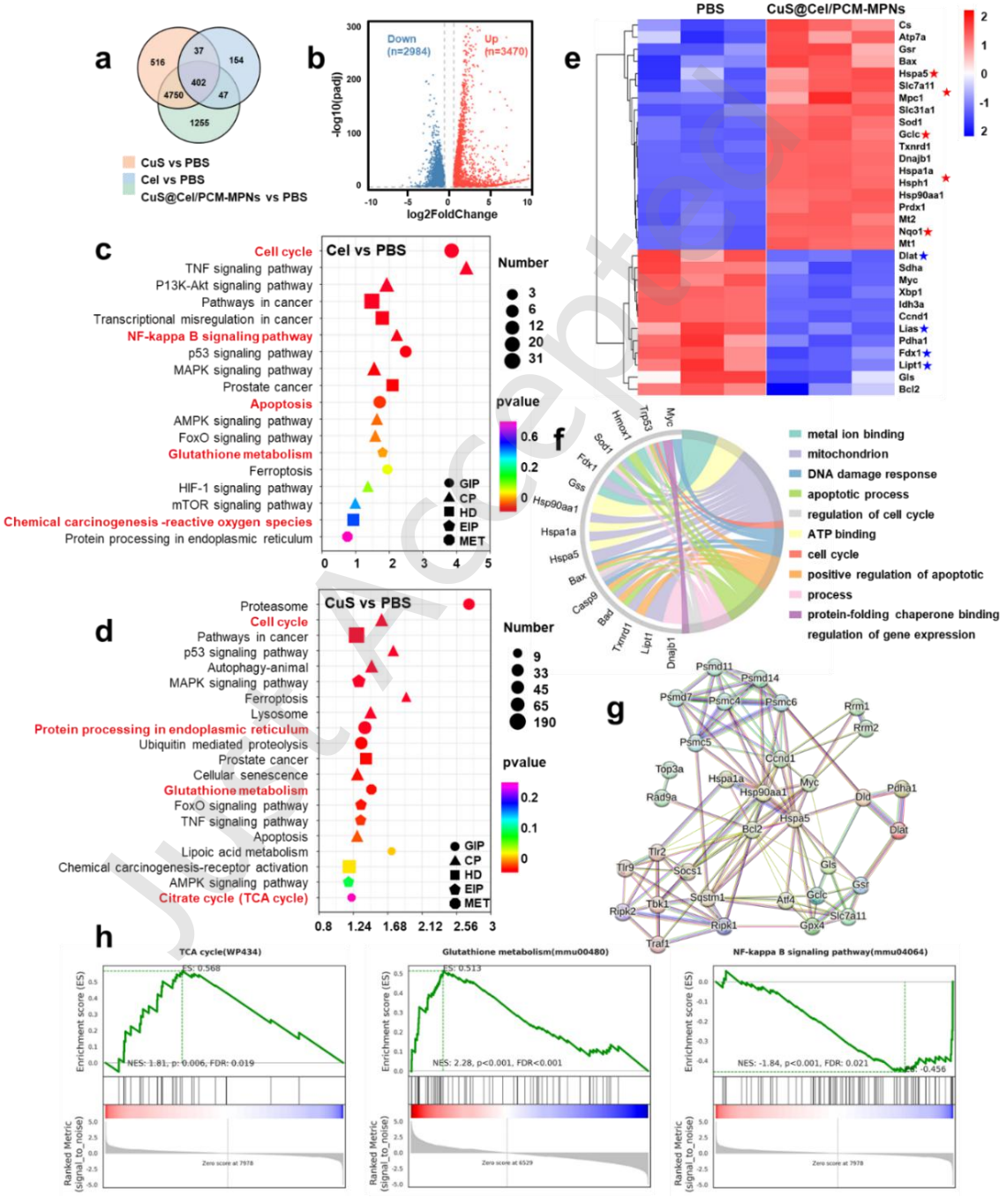

Figure 5. Transcriptomic analysis. (a) Venn diagram of differentially expressed genes. (b) Volcano plot of transcriptional changes. (c, d) KEGG enrichment for Cel vs PBS and CuS vs PBS. (e) Heat map of gene expressions in cells treated with PBS and CuS@Cel/PCM-MPNs. (f) GO chord diagram linking genes to functions. (g) Protein-protein interaction networks. (h) GSEA of TCA cycle, glutathione metabolism and NF-κB signaling pathways.

2.6 In vivo PA and MR imaging performance

As an integrated theranostic platform, CuS@Cel/PCM-MPNs were further evaluated for their in vivo imaging

capability. Benefiting from their strong absorption in the NIR-II region, the nanoparticles are well-suited for PA imaging. Prior to in vivo experiments, the hemocompatibility of CuS@Cel/PCM-MPNs was evaluated. The hemolysis rates at all tested concentrations were below 5%, indicating good biosafety for intravenous administration **(Figure S7)**.

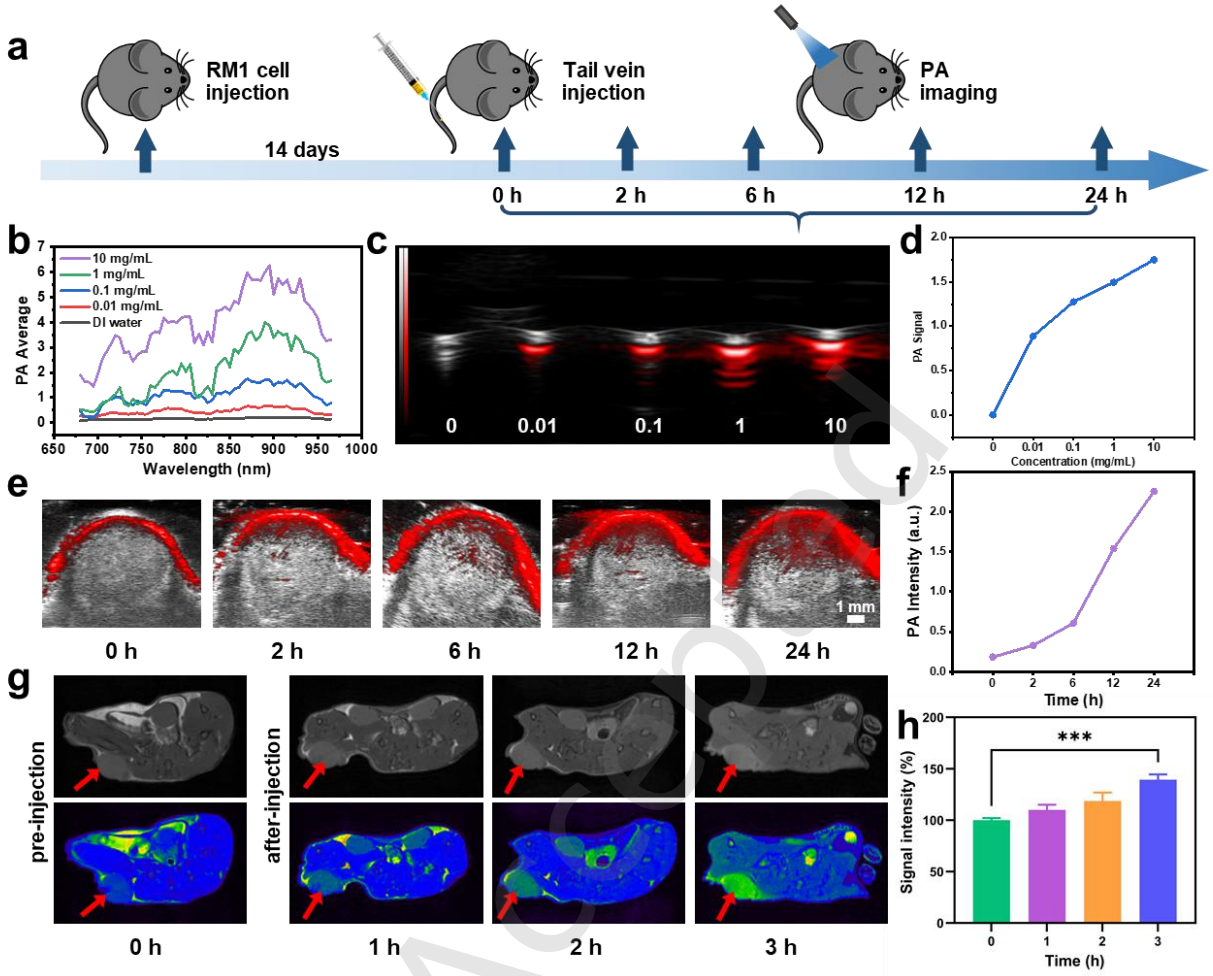

Figure 6. In vivo PA and MR imaging of CuS@Cel/PCM-MPNs. (a) Schematic illustration of the in vivo PA imaging procedure in RM1 tumor-bearing mice. (b) PA absorption spectrum of CuS@Cel/PCM-MPNs at different wavelengths. (c) PA images of CuS@Cel/PCM-MPNs at different concentrations. (d) Corresponding quantitative analysis of PA signal intensities. (e) In vivo PA images of RM1 tumor-bearing mice at different time points (0, 2, 6, 12, and 24 h) after intravenous injection of CuS@Cel/PCM-MPNs. (f) Quantitative analysis of PA signal intensities at the tumor site over time. (g) T_1-weighted MR images of RM1 tumor-bearing mice before and after intravenous injection of CuS@Cel/PCM-MPNs at different time points (0, 1, 2, and 3 h). (h) Corresponding quantitative analysis of MR signal intensities at the tumor region.

Following this, as illustrated in **Figure 6a**, RM1 tumor-bearing models were established by subcutaneous inoculation of RM1 cells into the thigh of C57BL/6 mice. After tumor growth for 14 days, the mice were intravenously injected with CuS@Cel/PCM-MPNs, and PA signals at the tumor site were recorded at different time points (0, 2, 6, 12, and 24 h). To first verify the intrinsic PA properties of the nanoplatform, its optical behavior was evaluated in vitro. The PA absorption spectrum of CuS@Cel/PCM-MPNs exhibited strong absorption in the near-infrared region **(Figure 6b)**. In addition, the PA signal intensity increased in a concentration-dependent manner **(Figure 6c, 6d)**, demonstrating their excellent PA imaging performance. Encouraged by these results, in vivo PA imaging was subsequently performed. A time-dependent enhancement of PA signals was observed at the tumor site, with a maximum signal at 24 h post-injection, suggesting efficient tumor accumulation of the nanoparticles. This tendency was further supported by quantitative analysis **(Figure 6e, 6f)**. Furthermore, due to the incorporation of Mn^{2+} within the MPNs, the nanoparticles also enabled T_1-weighted MR imaging[35]. As shown in **Figure 6g**, the MR signal at the tumor site was significantly enhanced after injection and increased over time (1-3 h), which showed a consistent trend in the quantitative analysis **(Figure 6h)**. Interestingly, the peak enhancement of MR signals occurred earlier than that of PA signals. This difference is mainly attributed to the distinct imaging mechanisms of the two modalities. PA imaging primarily depends on the accumulation of CuS nanoparticles within the tumor, which gradually increases through the enhanced permeability and retention (EPR) effect and therefore reaches its maximum intensity at a later time point (24 h). In contrast, T_1-weighted MR enhancement is mainly associated with the accessibility of Mn^{2+} species, whose longitudinal relaxation effect can be rapidly activated after nanoparticle accumulation and partial pH-responsive dissociation of the MPNs in the tumor microenvironment. Consequently, MR imaging provides earlier contrast enhancement, whereas PA imaging more accurately reflects the maximal tumor accumulation of the nanoplatform. These

complementary temporal characteristics further demonstrate the advantages of combining PA and MR imaging for monitoring nanoparticle delivery and optimizing the therapeutic time window.

2.7 In vivo antitumor therapeutic efficacy

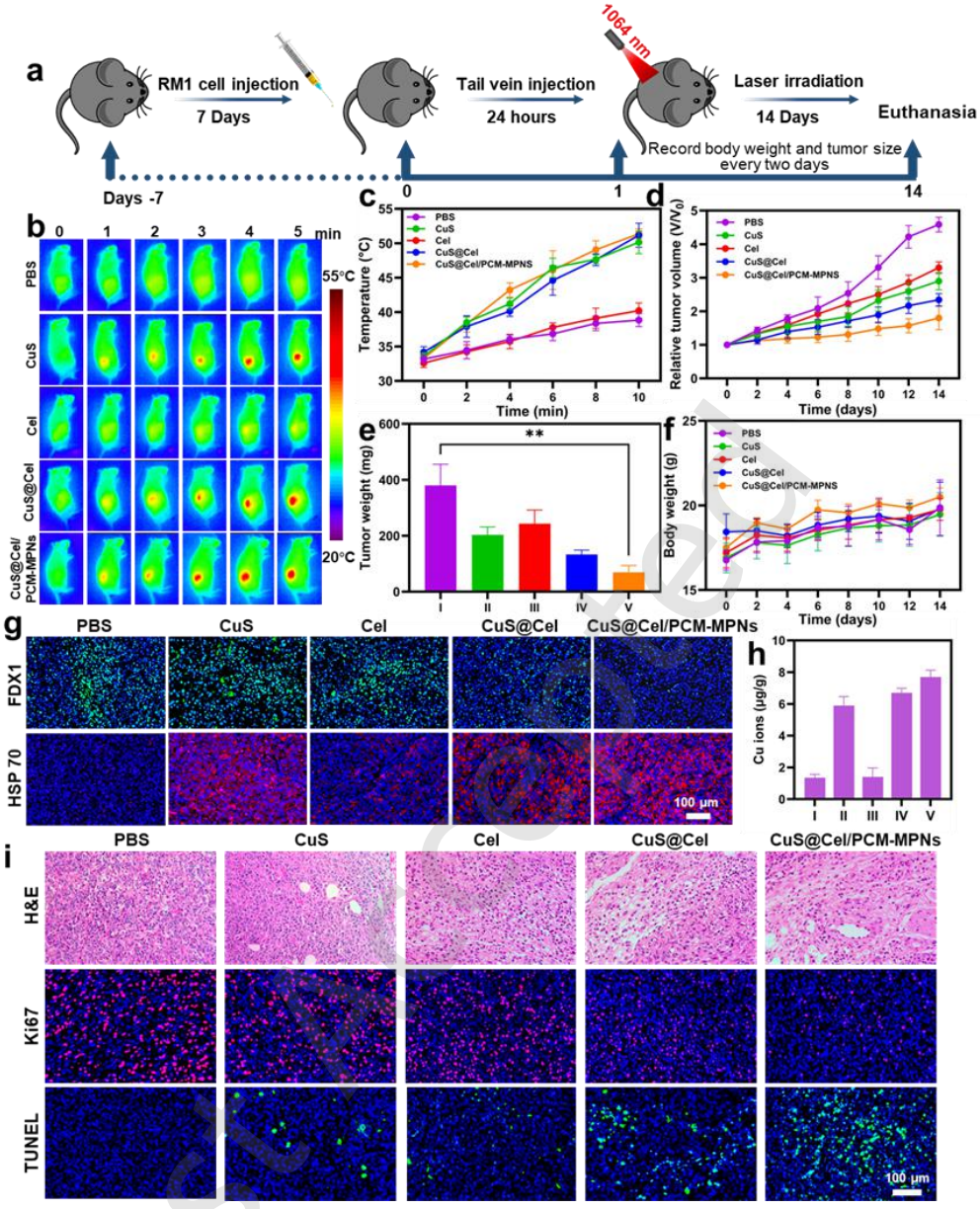

Figure 7. In vivo antitumor therapeutic efficacy of different formulations under 1064 nm laser irradiation. (a) Schematic illustration of the in vivo therapeutic protocol. RM1 tumor-bearing mice were randomly assigned to different treatment groups, and all treatment groups received identical 1064 nm laser irradiation following intravenous administration of the corresponding formulations. (b) Infrared thermal images of tumor-bearing mice under 1064 nm laser irradiation (1.0 W/cm^2, 5 min). (c) Temperature elevation curves at the tumor site during laser irradiation. (d) Relative tumor volume growth curves of different treatment groups under identical 1064 nm laser irradiation over 14 days. (e) Tumor weights of mice in different groups at the end of treatment. (f) Body weight changes of mice during the treatment period. (g) CLSM images of FDX1 and HSP70 immunofluorescence staining in tumors. (h) Quantitative analysis of Cu content in tumor tissues from different treatment groups determined by ICP-MS. (i) Representative H&E, Ki-67, and TUNEL staining images of tumor tissues from different groups.

The in vivo antitumor efficacy of CuS@Cel/PCM-MPNs was evaluated in RM1 tumor-bearing mice. As illustrated in **Figure 7a**, RM1 cells were subcutaneously inoculated into the thigh of C57BL/6 mice, and after 7 days when tumors reached an appropriate size, in order to distinguish the therapeutic effects of different formulations under the same photothermal conditions, the mice were randomly divided into five groups (PBS + laser, CuS + laser, Cel + laser, CuS@Cel + Laser, and CuS@Cel /PCM MPN + laser), followed by intravenous administration. After 24 h post-injection, the tumor sites were irradiated with a 1064 nm laser (1.0 W/cm^2, 5 min), and tumor volume and body weight were monitored every two days for 14 days. Infrared thermal imaging was employed to assess the photothermal effect in vivo. As shown in **Figure 7b**, the temperature at the tumor site in the CuS@Cel/PCM-MPNs group rapidly increased under laser irradiation, reaching approximately 50 °C, which was significantly higher than that of the control groups. The corresponding temperature-time curves further demonstrated a more pronounced heating profile **(Figure 7c)**, indicating efficient photothermal conversion and heat accumulation at the tumor site. The therapeutic efficacy was subsequently evaluated by tracking tumor growth. As shown in **Figure 7d**, tumors in the PBS group exhibited rapid

progression, whereas the growth rate in the CuS@Cel/PCM-MPNs group was markedly suppressed, with tumor growth being approximately fivefold slower than that of the PBS group. This significant inhibition was further corroborated by the final tumor weights, where the CuS@Cel/PCM-MPNs-treated group showed the lowest tumor burden among all groups **(Figure 7e)**. Importantly, throughout the treatment period, no significant changes in body weight were observed in any group **(Figure 7f)**, suggesting minimal systemic toxicity. Simultaneously, H&E staining of major organs showed no noticeable pathological abnormalities **(Figure S8)**, and blood routine and biochemical tests showed no significant differences among the control and treatment groups **(Figure S9, S10)**. This indicates that the nanoplatform possesses good biocompatibility and biosafety.

Immunofluorescence staining was performed to investigate the underlying therapeutic mechanisms **(Figure 7h)**. FDX1, a key regulator of mitochondrial metabolism involved in copper-dependent cell death, showed a progressive decrease in expression in the CuS-containing groups and reached the lowest level in the CuS@Cel/PCM-MPNs group, suggesting that mitochondrial metabolic dysregulation contributes to the induction of cuproptosis and the resulting antitumor efficacy[9, 19]. The consistent downregulation of FDX1 in tumor tissues agrees well with the in vitro findings, indicating that the cuproptosis-associated molecular alterations observed in cultured cells can also be reproduced in vivo, thereby further supporting the involvement of cuproptosis in the antitumor efficacy of CuS@Cel/PCM-MPNs. In contrast, HSP70, a classical heat shock protein indicative of thermal stress, was markedly upregulated upon laser irradiation, especially in the CuS@Cel/PCM-MPNs group, indicating efficient photothermal-induced thermal stress contributing to enhanced tumor ablation[6, 43]. To further verify the enhanced intratumoral copper delivery in vivo, the Cu content in tumor tissues was quantitatively analyzed by ICP-MS after treatment. As shown in **Figure 7h**, lower copper levels were detected in the PBS and the Cel groups, whereas the CuS-treated group showed increased Cu accumulation. Notably, CuS@Cel and CuS@Cel/PCM-MPNs exhibited progressively higher Cu levels, consistent with the intracellular copper accumulation observed in vitro. These results further support that the enhanced therapeutic efficacy is associated with increased intratumoral copper accumulation, providing additional evidence for the proposed cuproptosis mechanism. Subsequently, histological analysis was conducted to evaluate the therapeutic outcomes **(Figure 7i)**. H&E staining revealed extensive tumor tissue damage in the CuS@Cel/PCM-MPNs group. Meanwhile, Ki-67 staining showed a significant reduction in proliferative cells, and TUNEL staining exhibited a marked increase in apoptotic signals, further confirming the enhanced antitumor efficacy of the treatment[17].

3. Conclusion

In summary, we successfully developed a multifunctional CuS@Cel/PCM-MPNs nanoplatform integrating NIR-II photothermal therapy, stimuli-responsive drug release, catalytic activity, and dual-modal PA/MR imaging for synergistic prostate cancer theranostics. The hollow CuS structure enabled efficient Cel loading and strong photothermal conversion under 1064 nm irradiation, while the PCM and MPNs endowed the system with temperature- and pH-responsive release behavior. Under acidic and photothermal conditions, the nanosystem achieved responsive release of Cu ions and Cel, thereby synergistically disrupting intracellular redox homeostasis and mitochondrial function to amplify cuproptosis in tumor cells. Furthermore, the nanoplatform exhibited efficient tumor accumulation and excellent PA/MR imaging capability, enabling imaging-guided therapy. Both conventional 2D cell experiments and physiologically relevant 3D tumor spheroid studies, together with in vivo investigations, demonstrated potent antitumor efficacy against RM1 prostate tumors with minimal systemic toxicity and favorable biosafety. Collectively, this work provides a promising strategy for NIR-II photothermal-enhanced cuproptosis therapy and highlights the advantages of NIR-II-responsive nanoplatforms for precise prostate cancer treatment.

Electronic Supplementary Material: Supplementary material (materials and methods, other supplementary images) is available in the online version of this article at https://doi.org/10.26599/NR.2026.94909061.

Data availability

All data needed to support the conclusions in the paper are presented in the manuscript and/or the Electronic Supplementary Material. Additional data related to this paper may be requested from the corresponding author upon request.

Acknowledgements

We are thankful for financial support from the National Natural Science Foundation of China (No. 82272821), and the Fundamental Research Funds for the Central Universities (No. YG2025QNB30).

Declaration of competing interest

All the contributing authors report no conflict of interests in this work.

Author contribution statement

N. K.: Data curation, validation, writing manuscript, experimental design. Z. M. L.: Data curation, project administration, experimental design. F. T.: Validation, writing manuscript. H. S. T.: Project administration, funding acquisition. Q. Z.: Project administration, funding acquisition, review manuscript. All the authors have approved the final manuscript.

Informed consent

Not applicable

Ethics statement

All animal experiments were approved by the Institutional Animal Care and Use Committee of Shanghai Jiao Tong University (Ethical code: A2026094).

Use of AI statement

None

References

[1] R.L. Siegel, T.B. Kratzer, A.N. Giaquinto, H. Sung, A. Jemal, Cancer statistics, 2025, CA Cancer J. Clin. 75 (2025) 10–45.

[2] F. Bray, M. Laversanne, H. Sung, J. Ferlay, R.L. Siegel, I. Soerjomataram, A. Jemal, Global cancer statistics 2022: GLOBOCAN estimates of incidence and mortality worldwide for 36 cancers in 185 countries, CA Cancer J. Clin. 74 (2024) 229–263.

[3] G. Devos, W. Devlies, G. De Meerleer, M. Baldewijns, T. Gevaert, L. Moris, D. Milonas, H. Van Poppel, C. Berghen, W. Everaerts, F. Claessens, S. Joniau, Neoadjuvant hormonal therapy before radical prostatectomy in high-risk prostate cancer, Nat. Rev. Urol. 18 (2021) 739–762.

[4] N. Nussbaum, D.J. George, A.P. Abernethy, C.M. Dolan, N. Oestreicher, S. Flanders, T.B. Dorff, Patient experience in the treatment of metastatic castration-resistant prostate cancer: state of the science, Prostate Cancer Prostatic Dis. 19 (2016) 111–121.

[5] S. Zhang, T. Zhang, G.K. Kinsella, J.F. Curtin, A review of the efficacy of prostate cancer therapies against castration-resistant prostate cancer, Drug Discov. Today 30 (2025) 104384.

[6] J. Lu, Y. Miao, Y. Li, Cuproptosis: Advances in Stimulus-Responsive Nanomaterials for Cancer Therapy, Adv. Healthc. Mater. 13 (2024) 2400652.

[7] P. Tsvetkov, S. Coy, B. Petrova, M. Dreishpoon, A. Verma, M. Abdusamad, J. Rossen, L. Joesch-Cohen, R. Humeidi, R.D. Spangler, J.K. Eaton, E. Frenkel, M. Kocak, S.M. Corsello, S. Lutsenko, N. Kanarek, S. Santagata, T.R. Golub, Copper induces cell death by targeting lipoylated TCA cycle proteins, Science 375 (2022) 1254–1261.

[8] C. Xiong, H. Ling, Q. Hao, X. Zhou, Cuproptosis: p53-regulated metabolic cell death?, Cell Death Differ. 30 (2023) 876–884.

[9] L. Chen, J. Min, F. Wang, Copper homeostasis and cuproptosis in health and disease, Signal Transduct. Target. Ther. 7 (2022) 378.

[10] R. Cheng, Z. Li, W. Luo, H. Chen, T. Deng, Z. Gong, Q. Zheng, B. Li, Y. Zeng, H. Wang, C. Huang, A Copper-Based Photothermal-Responsive Nanoplatform Reprograms Tumor Immunogenicity via Self-Amplified Cuproptosis for Synergistic Cancer Therapy, Adv. Sci. 12 (2025) 2500652.

[11] Y. Xu, S.Y. Liu, L. Zeng, H. Ma, Y. Zhang, H. Yang, Y. Liu, S. Fang, J. Zhao, Y. Xu, C.R. Ashby, Y. He, Z. Dai, Y. Pan, An Enzyme-Engineered Nonporous Copper(I) Coordination Polymer Nanoplatform for Cuproptosis-Based Synergistic Cancer Therapy, Adv. Mater. 34 (2022) 2204733.

[12] S. Qiang, X. Hu, R. Li, W. Wu, K. Fang, H. Li, Y. Sun, S. Liang, W. Zhao, M. Wang, Y. Lin, S. Shi, C. Dong, CuS Nanoparticles-Loaded and Cisplatin Prodrug Conjugated Fe(III)-MOFs for MRI-Guided Combination of Chemotherapy and NIR-II Photothermal Therapy, ACS Appl. Mater. Interfaces 14 (2022) 36503–36514.

[13] D. Wang, F. Yuan, X. Deng, H. Li, S. Nie, Q. Liu, X. Wang, Engineering of 2D Ultrathin CuS-PMA Heterostructures for Enhanced NIR-II Photothermal Therapy Facilitating Oxidative Stress and Immunotherapy, Adv. Funct. Mater. 36 (2026) e27285.

[14] W. Chen, W. Xie, Z. Gao, C. Lin, M. Tan, Y. Zhang, Z. Hou, Mild-Photothermal Effect Induced High Efficiency Ferroptosis-Boosted-Cuproptosis Based on $Cu_2O@Mn_3Cu_3O_8$ Nanozyme, Adv. Sci. 10 (2023) 2303694.

[15] H. Sun, Y. Zhang, S. Chen, R. Wang, Q. Chen, J. Li, Y. Luo, X. Wang, H. Chen, Photothermal Fenton Nanocatalysts for Synergetic Cancer Therapy in the Second Near-Infrared Window, ACS Appl. Mater. Interfaces 12 (2020) 30145–30154.

[16] W. Li, Y. Wang, H. Yu, X. Zhang, Z. Ju, W. Zhao, R. Lv, Enhanced photothermal/immunotherapy under NIR irradiation based on hollow mesoporous responsive nanomotor, Inorg. Chem. 64.1 (2024) 495-509.

[17] G. Ku, M. Zhou, S. Song, Q. Huang, H. John, C. Li, Copper sulfide nanoparticles as a new class of photoacoustic contrast agent for deep tissue imaging at 1064 nm, ACS Nano 6 (2012) 7489–7496.

[18] C. Huang, B. Lin, C. Chen, H. Wang, X. Lin, J. Liu, Q. Ren, J. Tao, P. Zhao, Y. Xu, Synergistic Reinforcing of Immunogenic Cell Death and Transforming Tumor-Associated Macrophages Via a Multifunctional Cascade Bioreactor for Optimizing Cancer Immunotherapy, Adv. Mater. 34 (2022) 2207593.

[19] Y. Cao, X. Zhao, Y. Miao, X. Liu, X. Liu, Z. Yue, X. Ruan, Q. Tu, X. Wang, G. Zhou, J. Hu, D. Deng, Bilayer self-assembly encapsulated by engineered vesicle disrupts glutathione to induce Disulfidptosis-enhanced cuproptosis for tumor immunotherapy, J. Control. Release 387 (2025) 114232.

[20] A. Bishayee, G. Sethi, Bioactive natural products in cancer prevention and therapy: Progress and promise, Semin. Cancer Biol. 40–41 (2016) 1–3.

[21] N. Qiu, Y. Liu, Q. Liu, Y. Chen, L. Shen, M. Hu, X. Zhou, Y. Shen, J. Gao, L. Huang, Celastrol nanoemulsion induces immunogenicity and downregulates PD-L1 to boost abscopal effect in melanoma therapy, Biomaterials 277 (2021) 121121.

[22] L. An, Z. Li, L. Shi, L. Wang, Y. Wang, L. Jin, X. Shuai, J. Li, Inflammation-Targeted Celastrol Nanodrug Attenuates Collagen-Induced Arthritis through NF-κB and Notch1 Pathways, Nano Lett. 20 (2020) 7728–7736.

[23] Y. Li, N. Wang, H. Li, X. Zhang, L. Meng, Y. Yu, S. Wang, L. Deng, Biomineralization of Copper-Celastrol Nanohybrids for Synergistic Antitumor Therapy, Small 21 (2025) 2412802.

[24] S. Lu, Y. Li, Y. Yu, Glutathione-Scavenging Celastrol-Cu Nanoparticles Induce Self-Amplified Cuproptosis for Augmented Cancer Immunotherapy, Adv. Mater. 36 (2024) 2404971.

[25] W. Chen, P. Sheng, Y. Chen, Y. Liang, S. Wu, L. Jia, X. He, C. Zhang, C. Wang, C. Yuan, Hypoxia-responsive immunostimulatory nanomedicines synergize with checkpoint blockade immunotherapy for potentiating cancer immunotherapy, Chem. Eng. J. 451 (2023) 138781.

[26] L. Wu, W. Pi, X. Huang, L. Yang, X. Zhang, J. Lu, S. Yao, X. Lin, X. Tan, Z. Wang, P. Wang, Orchestrated metal-coordinated carrier-free celastrol hydrogel intensifies T cell activation and regulates response to immune checkpoint blockade for synergistic chemo-immunotherapy, Biomaterials 312 (2025) 122723.

[27] K. Weng, X. Xu, Y. Chen, X. Li, C. Qing, D. Zou, Development and applications of multifunctional microencapsulated PCMs: A comprehensive review, Nano Energy 122 (2024) 109308.

[28] L.L. Fedoryshin, A.J. Tavares, E. Petryayeva, S. Doughan, U.J. Krull, Near-Infrared-Triggered Anticancer Drug Release from Upconverting Nanoparticles, ACS Appl. Mater. Interfaces 6 (2014) 13600–13606.

[29] Q. Li, L. Sun, M. Hou, Q. Chen, R. Yang, L. Zhang, Z. Xu, Y. Kang, P. Xue, Phase-Change Material Packaged within Hollow Copper Sulfide Nanoparticles Carrying Doxorubicin and Chlorin e6 for Fluorescence-Guided Trimodal Therapy of Cancer, ACS Appl. Mater. Interfaces 11 (2019) 417–429.

[30] S.W. Choi, Y. Zhang, Y. Xia, A Temperature-Sensitive Drug Release System Based on Phase-Change Materials, Angew. Chem. Int. Ed. 49 (2010) 7904–7908.

[31] W. Zhang, Q.A. Besford, A.J. Christofferson, P. Charchar, J.J. Richardson, A. Elbourne, K. Kempe, C.E. Hagemeyer, M.R. Field, C.F. McConville, I. Yarovsky, F. Caruso, Cobalt-Directed Assembly of Antibodies onto Metal–Phenolic Networks for Enhanced Particle Targeting, Nano Lett. 20 (2020) 2660–2666.

[32] Z. Tang, Z. Huang, Y. Huang, M. Huang, H. Liu, J. Du, B. Jia, Nanomedicine's shining armor: understanding and leveraging the metal-phenolic networks, J. Nanobiotechnol. 23 (2025) 158.

[33] S. Xue, W. Tan, S. Mao, H. Pan, X. Ye, N. Donlao, J. Tian, Polyphenol-Based Functional Materials: Structural Insights, Composite Strategies, and Biomedical Applications, Adv. Sci. 12 (2025) e08924.

[34] Y. Guo, Q. Sun, F.G. Wu, Y. Dai, X. Chen, Polyphenol-Containing Nanoparticles: Synthesis, Properties, and Therapeutic Delivery, Adv. Mater. 33 (2021) 2007356.
[35] X. Pang, C. Fu, J. Chen, M. Su, R. Wei, Y. Wang, W. Lin, X. Wei, X. Jiang, X. Yang, H. Yang, J. Wang, R. Yang, A manganese-phenolic network platform amplifying STING activation to potentiate MRI guided cancer chemo-/chemodynamic/immune therapy, Biomater. Sci. 11 (2023) 3840–3850.
[36] W. Jiang, Q. Wang, D. Cui, L. Han, L. Chen, J. Xu, N. Niu, Metal-polyphenol network coated magnetic hydroxyapatite for pH-activated MR imaging and drug delivery, Colloids Surf. B: Biointerfaces 222 (2023) 113076.
[37] Z. Ouyang, D. Li, Z. Xiong, C. Song, Y. Gao, R. Liu, M. Shen, X. Shi, Antifouling Dendrimer-Entrapped Copper Sulfide Nanoparticles Enable Photoacoustic Imaging-Guided Targeted Combination Therapy of Tumors and Tumor Metastasis, ACS Appl. Mater. Interfaces 13 (2021) 6069–6080.
[38] C. Zhang, W. Sun, Y. Wang, F. Xu, J. Qu, J. Xia, M. Shen, X. Shi, Gd-/CuS-Loaded Functional Nanogels for MR/PA Imaging-Guided Tumor-Targeted Photothermal Therapy, ACS Appl. Mater. Interfaces 12 (2020) 9107–9117.
[39] S. Liang, X. Deng, Y. Chang, C. Sun, S. Shao, Z. Xie, X. Xiao, P.A. Ma, H. Zhang, Z. Cheng, J. Lin, Intelligent Hollow Pt-CuS Janus Architecture for Synergistic Catalysis-Enhanced Sonodynamic and Photothermal Cancer Therapy, Nano Lett. 19 (2019) 4134–4145.
[40] Y. Du, D. Liu, M. Sun, G. Shu, J. Qi, Y. You, Y. Xu, K. Fan, X. Xu, F. Jin, J. Wang, Q. Shen, L. Zhu, X. Ying, J. Ji, L. Wu, Multifunctional Gd-CuS loaded UCST polymeric micelles for MR/PA imaging-guided chemo-photothermal tumor treatment, Nano Res. 15 (2022) 2288–2299.
[41] Y. Jin, J. Huang, Y. Tang, Z. Li, A. Zhang, Z. Yang, J. Song, X. Huang, Y. Bai, C. Sun, X. Wu, J. Cheng, L. Wang, Q. Zhang, W. Yao, Boosting ferroptosis by intervention of redox balance and synergetic with photothermal/photodynamic therapy for suppression of pancreatic cancer, Chem. Eng. J. 497 (2024) 154569.
[42] E.J. Ge, A.I. Bush, A. Casini, P.A. Cobine, J.R. Cross, G.M. DeNicola, Q.P. Dou, K.J. Franz, V.M. Gohil, S. Gupta, S.G. Kaler, S. Lutsenko, V. Mittal, M.J. Petris, R. Polishchuk, M. Ralle, M.L. Schilsky, N.K. Tonks, L.T. Vahdat, L. Van Aelst, D. Xi, P. Yuan, D.C. Brady, C.J. Chang, Connecting copper and cancer: from transition metal signalling to metalloplasia, Nat. Rev. Cancer 22 (2022) 102–113.
[43] J. Yao, F. Yang, F. Zheng, C. Yao, J. Xing, X. Xu, A. Wu, Boosting Chemodynamic Therapy via a Synergy of Hypothermal Ablation and Oxidation Resistance Reduction, ACS Appl. Mater. Interfaces 13 (2021) 54770–54782.

Electronic Supplementary Material

CuS-based nanoplatform for NIR-II photothermal-enhanced and celastrol-boosted cuproptosis in prostate cancer

Nan Kang [1, §], Zimei Liu [2, §], Fu Tan [1], Haisong Tan [3], and Qian Zhang [1]

[1] *School of Automation and Intelligent Sensing, Shanghai Jiao Tong University, 800 Dongchuan RD, Shanghai 200240, China*
[2] *Department of Oncology, Tongren Hospital, Shanghai Jiao Tong University School of Medicine, Shanghai 200050, P.R. China*
[3] *Department of Urology, Shanghai Ninth People's Hospital Affiliated to Shanghai Jiao Tong University School of Medicine, Shanghai 200011, China*
[§] *Nan Kang and Zimei Liu contributed equally to this work.*

Address correspondence to Qian Zhang, qianzhang0130@sjtu.edu.c; Haisong Tan, tanhaisong1983@foxmail.com

Supporting information to https://doi.org/10.26599/NR.2026.94909061

Materials and methods

1. Materials

Polyvinylpyrrolidone (PVP K30, Mw = 40,000) was purchased from Psaitong Biotechnology Co., Ltd. (Shanghai, China). Copper(II) chloride dihydrate ($CuCl_2 \cdot 2H_2O$), sodium hydroxide (NaOH), L-ascorbic acid (AA), ethanol, and 1-tetradecanol were obtained from Sinopharm Chemical Reagent Co., Ltd. (Shanghai, China). Sodium sulfide (Na_2S) was purchased from Macklin Reagent Co., Ltd. (Shanghai, China).

Celastrol (Cel), dimethyl sulfoxide (DMSO), tannic acid (TA), tetramethylbenzidine (TMB), and rhodamine B hydrazide were obtained from Shanghai Aladdin Biochemical Technology Co., Ltd. (Shanghai, China). Manganese(II) chloride tetrahydrate ($MnCl_2 \cdot 4H_2O$, 99%) was purchased from Meryer Chemical Technology Co., Ltd. (Shanghai, China).

2',7'-Dichlorodihydrofluorescein diacetate (H_2DCFDA) was obtained from Merck KGaA (Darmstadt, Germany). Hoechst 33342, LysoTracker Green DND-26, Cy5.5 dye, and DAPI were purchased from Yeasen Biotechnology Co., Ltd. (Shanghai, China).

The Calcein-AM/propidium iodide (PI) kit and Cell Counting Kit-8 (CCK-8) were obtained from Dojindo Laboratories (Shanghai, China). The glutathione (GSH) assay kit was purchased from Nanjing Jiancheng Bioengineering Institute (Nanjing, China).

U-shaped ultra-low attachment 96-well plates were purchased from Corning Inc. (Corning, NY, USA). Cell culture reagents were obtained from Gibco (Thermo Fisher Scientific, Waltham, MA, USA).

For Western blot analysis, all reagents were purchased from Servicebio Biotechnology Co., Ltd. (Wuhan, China). The primary antibodies against DLAT (and other indicated proteins, e.g., FDX1, HSP70 if applicable) and corresponding secondary antibodies were obtained from Yeasen Biotechnology Co., Ltd. (Shanghai, China).

All chemicals were of analytical grade and used as received without further purification.

2. Materials Synthesis

Synthesis of Cu_2O: Polyvinylpyrrolidone (PVP, 0.6 g) and $CuCl_2 \cdot 2H_2O$ (0.0852 g) were dissolved in 20 mL of deionized (DI) water. Subsequently, NaOH (0.32 g) was added under magnetic stirring. After stirring for 5 min, ascorbic acid (0.1761 g) was introduced and the mixture was further stirred for 5 min. The solution gradually turned orange, indicating the formation of Cu_2O. The product was collected by centrifugation at 6000 rpm for 5 min, washed twice with absolute ethanol and twice with DI water, and finally redispersed in 10 mL of DI water to obtain a Cu_2O suspension.

Synthesis of CuS: An aliquot (1 mL) of the above-prepared Cu_2O suspension was heated to 90 °C under continuous stirring. Then, Na_2S (0.00976 g) was added, and the reaction was maintained for 50 min. After completion, the product was collected by centrifugation at 6000 rpm for 5 min and washed with DI water to obtain CuS. After drying, the obtained CuS nanoparticles were weighed to determine the recovery yield of the conversion process, which was used as the basis for subsequent surface modification and drug loading steps.

Synthesis of CuS@Cel: CuS (50 mg) was prepared as described above and dispersed in 10 mL of dimethyl sulfoxide (DMSO). A 10 mM Celastrol (Cel) solution in DMSO was prepared, and 1 mL of this solution was added to the CuS dispersion. The mixture was stirred overnight. The product was collected by centrifugation at 6000 rpm for 5 min and washed with DI water to obtain CuS@Cel. The recovered CuS@Cel product was dried and weighed, and the mass recovery was recorded to evaluate the efficiency of the Cel-loading process. The Cel loading content was further calculated based on the UV–vis calibration curve, with an encapsulation efficiency of 78.94%.

Synthesis of CuS@Cel/PCM: CuS@Cel (40 mg) and 1-tetradecanol (67 mg) were added to 70 mL of DI water and stirred at 55 °C for 1 h. The resulting product was collected by centrifugation at 6000 rpm for 10 min and washed twice with ice-cold water to obtain CuS@Cel/PCM.

Synthesis of CuS@Cel/PCM-MPNs: CuS@Cel/PCM (18 mg) was dispersed in 6 mL of DI water using ultrasonication. Then, 200 μL of tannic acid (TA, 40 mg/mL) aqueous solution was added, followed by ultrasonication and stirring for 2 min. Subsequently, 200 μL of $MnCl_2$ aqueous solution (10 mg/mL) was added and stirred for 5 min. After that, 600 μL of phosphate-buffered saline (PBS) was introduced, and the reaction mixture was stirred overnight. Finally, the product was collected by centrifugation at 10,000 rpm for 5 min and washed twice with DI water to obtain CuS@Cel/PCM-MPNs. The final CuS@Cel/PCM-MPNs product was collected, dried, and weighed to determine the overall recovery mass after stepwise coating. The obtained mass was used for calculating the corresponding administration dose in the subsequent animal experiments. The final dried CuS@Cel/PCM-MPNs were weighed after purification. Based on the recovered mass and Cel loading content (6.6%), the final formulation contained approximately 6.6 wt% Cel.

In particular, the packaging efficiency (EE) is calculated according to eq 1:

$$EE\% = \frac{Weight\ of\ Cel\ in\ nanosystem}{Weight\ of\ Cel\ added\ initially} \quad (1)$$

3. Characterization

The morphology and size distribution of the nanoparticles (NPs) were characterized by transmission electron microscopy (TEM, Talos F200X G2, Thermo Fisher Scientific, Waltham, MA, USA). The surface morphology was further examined using field-emission scanning electron microscopy (FESEM, JSM-7800F, JEOL, Tokyo, Japan). X-ray diffraction (XRD) patterns were recorded on an X-ray diffractometer (D8 ADVANCE Da Vinci, Bruker, Karlsruhe, Germany). The surface chemical compositions and valence states were analyzed by X-ray photoelectron spectroscopy (XPS, AXIS UltraDLD, Kratos Analytical, Manchester, UK), and the spectra were processed using CasaXPS software. The UV–vis–NIR absorption spectra of various samples were measured using a UV–vis spectrophotometer (UH5700, Hitachi, Tokyo, Japan). The hydrodynamic diameter and zeta potential of the nanoparticles were determined by dynamic light scattering (DLS) using a Zeta Potential/Particle Sizer (Omni, USA).

4. In Vitro Photothermal Performance Study

CuS and CuS@Cel/PCM-MPNs were dispersed in deionized water to obtain solutions with different concentrations (0.1, 0.25, and 0.5 mg/mL). Aliquots (200 μL) of each solution were transferred into 0.5 mL centrifuge tubes and irradiated with a 1064 nm laser

at a power density of 1.0 W/cm^2 for 300 s. The temperature of the solutions was recorded every 30 s using an infrared thermal imaging camera, and the corresponding heating curves were obtained. Deionized water was used as a control under identical conditions. To investigate the effect of laser power density, the concentration of CuS@Cel/PCM-MPNs was fixed at 0.5 mg/mL and irradiated with a 1064 nm laser at different power densities (0.8, 1.0, and 1.2 W/cm^2) for 300 s. The temperature variation was recorded at 30 s intervals. For photothermal stability evaluation, the as-prepared CuS@Cel/PCM-MPNs solution (0.5 mg/mL) was subjected to four laser on/off cycles under 1064 nm irradiation (1.0 W/cm^2). Each cycle consisted of a heating period followed by natural cooling. The total duration was 2400 s, and temperature changes were continuously monitored.

5. In Vitro Release and Catalytic Properties of the Material

Cel Standard Curve: A series of Cel aqueous solutions (0.002–0.0125 mM) were prepared. The absorbance at 422 nm was measured using a UV–vis spectrophotometer, and a calibration curve was established based on the corresponding optical density (OD) values.

Cu^{2+} and Cel Release Behavior: CuS@Cel/PCM-MPNs were dispersed in buffer solutions to obtain a stock concentration of 0.2 mg/mL. Release experiments were performed in phosphate-buffered saline (PBS, pH 7.4) and citrate buffer (pH 5.0) under four conditions: pH 7.4, pH 7.4 with laser irradiation, pH 5.0, and pH 5.0 with laser irradiation. For laser-treated groups, samples were exposed to a 1064 nm laser (1.0 W/cm^2) for 5 min, while non-irradiated samples were maintained at room temperature. At predetermined time intervals (up to 7 h), aliquots were collected for analysis. The released Cu^{2+} ions were quantified using inductively coupled plasma mass spectrometry (ICP–MS, Thermo Fisher Scientific). For Cel release, the supernatant was collected after centrifugation, and the absorbance was measured using a UV–vis spectrophotometer. The drug concentration was calculated based on the standard curve, and the cumulative release was determined using the equation $(C_t \times V)/m$, where C_t is the measured drug concentration, V is the total volume, and m is the initial drug loading.

Fenton Catalytic Activity: The Fenton-like catalytic activity of CuS@Cel/PCM-MPNs was evaluated using tetramethylbenzidine (TMB) as a chromogenic substrate. Typically, buffer solution (450 μL, pH 5.0-7.0), CuS@Cel/PCM-MPNs (200 μg/mL, 5 μL), TMB (0.5 mM, 5 μL), and H_2O_2 (0.5 mM, 5 μL unless otherwise specified) were mixed to initiate the reaction. The absorbance at 650 nm was recorded every 30 s using a UV–vis spectrophotometer to monitor the oxidation of TMB. To investigate the catalytic performance under different conditions, experiments were conducted by varying (i) pH (5.0, 6.0, and 7.0), (ii) H_2O_2 concentration (0.3–0.5 mM), and (iii) temperature. For photothermal-enhanced catalysis, the temperature was increased to ~55 °C by irradiation with a 1064 nm laser (1.0 W/cm^2) for 5 min. Control groups including TMB alone, TMB + NPs, and TMB + H_2O_2 were evaluated under identical conditions.

6. In vitro cell uptake

Fluorescent Labeling of Nanoparticles: CuS@Cel/PCM-MPNs (10 mL, 10 μg/mL) were prepared in deionized water. Cy5.5 (0.01 mg) was dissolved in 1 mL of dimethyl sulfoxide (DMSO) and added dropwise to the nanoparticle suspension under stirring. The mixture was stirred for 2 h at room temperature, followed by centrifugation (6000 rpm, 5 min) to remove excess dye. The precipitate was washed and redispersed in deionized water to obtain Cy5.5-labeled nanoparticles at a final concentration of 30 μg/mL.

Cellular Uptake Study: Cellular uptake of the Cy5.5-labeled nanoparticles was observed using a confocal laser scanning microscopy system (CLSM, STELLARIS 5, Leica, Wetzlar, Germany). RM1 cells were seeded in 14 mm glass-bottom dishes (1×10^5 cells per well) and cultured for 24 h under standard conditions (37 °C, 5% CO_2). The cells were then incubated with Cy5.5-labeled nanoparticles for different time periods (1, 3, and 5 h). After incubation, the cells were washed three times with PBS to remove extracellular nanoparticles. The nuclei were stained with Hoechst 33342 (10 μg/mL) for 10 min in the dark. After washing with PBS, the cells were maintained in fresh PBS and imaged by CLSM. The excitation/emission wavelengths were set as follows: Hoechst 33342 (λex: 405 nm / λem: 420–470 nm), Lysotracker Green DND-26 (λex: 488 nm / λem: 500–550 nm), Cy5.5 (λex: 640 nm / λem: 680–740 nm).

3D Tumor Spheroid Penetration: To evaluate tumor penetration, three-dimensional (3D) tumor spheroids were established using RM1 cells. Briefly, RM1 cells (5×10^3 cells per well) were seeded into U-shaped ultra-low attachment 96-well plates and cultured for 5 days to form compact spheroids. The spheroids were then incubated with Cy5.5-labeled nanoparticles for different time intervals (1, 3, and 5 h). After incubation, the spheroids were washed with PBS and directly imaged using CLSM. Cy5.5 (λex: 640 nm/λem: 680–740 nm).

7. In Vitro Cytotoxicity

CCK-8 Assay: RM1 cells were seeded into 96-well plates at a density of 5.0×10^3 cells per well and cultured for 24 h at 37 °C in a 5% CO_2 atmosphere. The cells were then treated with CuS, Cel, CuS@Cel, and CuS@Cel/PCM-MPNs at different concentrations (final Cel concentration: 1 μg/mL) for 24 h. After incubation, the culture medium was removed, and the cells were washed with PBS and replenished with fresh complete medium. The cells were subsequently exposed to 1064 nm laser irradiation (1.0 W/cm^2) for 5 min. After irradiation, the cells were further incubated for 12 h. Then, 100 μL of fresh medium containing 10 μL of CCK-8 reagent was added to each well, followed by incubation in the dark for 2 h. The absorbance at 450 nm was measured using a microplate reader. Cell viability was calculated according to the following eq 2:

$$Cellviability(\%) = \frac{(OD_{Treaded} - OD_{Blank})}{(OD_{Control} - OD_{Blank})} \times 100\% \quad (2)$$

Live/Dead Cell Staining: RM1 cells were seeded in 14 mm confocal dishes at a density of 1×10^5 cells per well and cultured for 24 h. The cells were then treated with different formulations (CuS, Cel, CuS@Cel, and CuS@Cel/PCM-MPNs; final Cel concentration: 1 μg/mL) for 12 h. After incubation, the medium was replaced with fresh culture medium. A portion of the cells was subjected to 1064 nm laser irradiation (1.0 W/cm^2, 5 min), followed by further incubation for 12 h. Subsequently, the cells were washed with PBS and stained with Calcein AM (2.0 μM) and propidium iodide (PI, 1.5 μM) for 40 min in the dark. After staining, the cells were observed using a confocal laser scanning microscope (CLSM). The excitation/emission wavelengths were set as follows: Calcein AM (λex = 488 nm, λem = 500–520 nm) and PI (λex = 488 nm, λem = 600–620 nm).

3D Tumor Spheroid Viability Assay: RM1 cells were seeded into U-shaped ultra-low attachment 96-well plates at a density of 5×10^3 cells per well and cultured for 5 days to form 3D tumor spheroids. The spheroids were then incubated with different formulations (CuS, Cel, CuS@Cel, and CuS@Cel/PCM-MPNs; final Cel concentration: 1 μg/mL) for 24 h. Subsequently, part of the spheroids was irradiated with a 1064 nm laser (1.0 W/cm^2, 5 min) and further cultured for 12 h. After treatment, the spheroids were washed with PBS and stained with Calcein AM (2.0 μM) and PI (8 μM) for 1 h. The stained spheroids were imaged using CLSM. The excitation/emission wavelengths were set as follows: Calcein AM (λex = 488 nm, λem = 500–520 nm) and PI (λex = 488 nm, λem = 600–620 nm).

8. In Vitro Fluorescence Assay of Intracellular Copper Ions

Intracellular Cu^{2+} levels were evaluated using the copper-sensitive fluorescent probe rhodamine B hydrazide. RM1 cells were seeded in 14 mm confocal dishes at a density of 1×10^5 cells per well and cultured for 24 h under standard conditions. The cells were divided into five groups: PBS, CuS, Cel, CuS@Cel, and CuS@Cel/PCM-MPNs (final Cel concentration: 1 μg/mL), and incubated for 12 h. After treatment, the cells were washed with PBS and incubated with rhodamine B hydrazide (10 μM) for 30 min. Subsequently, the cells were washed with PBS and stained with Hoechst 33342 (10 μg/mL) for 10 min in the dark. After three washes with PBS, the cells were maintained in PBS and imaged using a confocal laser scanning microscope (CLSM). Rhodamine B hydrazide (λex: 561 nm, λem: 570–630 nm) and Hoechst 33342 (λex: 405 nm, λem: 420–470 nm).

9. In Vitro Measurement of Cellular ROS and GSH

Intracellular reactive oxygen species (ROS) levels were evaluated using the ROS-sensitive probe H_2DCFDA. RM1 cells were seeded in 14 mm confocal dishes at a density of 1×10^5 cells per well and cultured for 24 h. The cells were divided into five groups: PBS, CuS, Cel, CuS@Cel, and CuS@Cel/PCM-MPNs (final Cel concentration: 1 μg/mL) and incubated for 12 h. After treatment, the medium was replaced, and a portion of the cells was exposed to 1064 nm laser irradiation (1.0 W/cm^2, 5 min), followed by further incubation for 12 h at 37°C. Subsequently, the cells were incubated with H_2DCFDA (10 μM) for 25 min at 37°C in the dark. After washing with PBS, the nuclei were stained with Hoechst 33342 (10 μg/mL) for 10 min. The cells were then washed three times with PBS and imaged using a confocal laser scanning microscope (CLSM). The excitation/emission wavelengths were set as follows: H_2DCFDA (λex = 488 nm, λem = 510–530 nm) and Hoechst 33342 (λex = 405 nm, λem = 420–470 nm).

To further assess intracellular redox homeostasis, glutathione (GSH) levels were measured. RM1 cells were seeded in 6-well plates at a density of 4×10^5 cells per well. After incubation, the cells were treated with CuS, Cel, CuS@Cel, or CuS@Cel/PCM-MPNs (final Cel concentration: 1 μg/mL) for 2 h, with untreated cells serving as the control group. Following treatment, intracellular GSH and oxidized glutathione (GSSG) were quantified using a commercial assay kit (Nanjing Jiancheng Bioengineering Institute) according to the manufacturer's instructions.

10. Western blot

RM1 cells were seeded in 6-well plates at a density of 1×10^6 cells per well and allowed to adhere overnight. The cells were then treated with CuS, Cel, CuS@Cel, or CuS@Cel/PCM-MPNs (final Cel concentration: 1 μg/mL) for 12 h. Subsequently, a portion of the cells was exposed to 1064 nm laser irradiation (1.0 W/cm^2, 5 min), followed by further incubation for 12 h at 37°C. After treatment, the cells were washed three times with cold PBS and lysed using RIPA buffer containing protease and phosphatase inhibitors. The lysates were collected and centrifuged at 12,000 rpm for 10 min at 4°C, and the supernatants were obtained for protein analysis. Protein concentrations were determined using a BCA protein assay kit. Equal amounts of protein were separated by SDS-PAGE and transferred onto PVDF membranes. The membranes were blocked and incubated with primary antibodies against target proteins overnight at 4°C, followed by incubation with HRP-conjugated secondary antibodies for 1 h at room temperature. Finally, the protein bands were visualized using an enhanced chemiluminescence (ECL) detection system.

11. Cellular DLAT Detection

To evaluate cuproptosis-related protein aggregation, dihydrolipoamide S-acetyltransferase (DLAT) expression was analyzed by immunofluorescence staining. RM1 cells were seeded in 14 mm confocal dishes at a density of 1×10^5 cells per well and cultured for 24 h. The cells were treated with CuS, Cel, CuS@Cel, or CuS@Cel/PCM-MPNs (final Cel concentration: 1 μg/mL) for 12 h. Subsequently, the cells was exposed to 1064 nm laser irradiation (1.0 W/cm^2, 5 min), followed by further incubation for 12 h at 37°C. After treatment, the cells were washed with PBS, fixed with 4% paraformaldehyde, and permeabilized with 0.05% Triton X-100. The cells were then blocked with 1% bovine serum albumin (BSA) and incubated with primary antibodies against DLAT overnight at 4°C. After washing, the cells were incubated with Alexa Fluor 488-conjugated secondary antibodies for 1 h at room temperature in the dark. The nuclei were counterstained with DAPI, and fluorescence images were acquired using a confocal laser scanning microscope (CLSM). The excitation/emission wavelengths were set as follows: DAPI (λex = 405 nm, λem = 420–480 nm) and Alexa Fluor 488 (λex = 488 nm, λem = 500–550 nm).

12. Transcriptome Analysis

RM1 cells were seeded in 6-well plates at a density of 1×10^6 cells per well and allowed to adhere overnight. The cells were then treated with CuS, Cel, CuS@Cel, or CuS@Cel/PCM-MPNs (final Cel concentration: 1 μg/mL) for 12 h. Subsequently, the cells were exposed to 1064 nm laser irradiation (1.0 W/cm^2, 5 min) and further incubated for 12 h. After treatment, the cells were harvested for RNA extraction. Total RNA extraction, reverse transcription, library preparation, and high-throughput sequencing were performed by Novogene Co., Ltd. (Beijing, China) following standard protocols. Differentially expressed genes (DEGs) were identified based on a threshold of $|\log_2$ fold change$| \geq 1$ and $p < 0.05$. Functional enrichment analyses, including Gene Ontology (GO) and Kyoto Encyclopedia of Genes and Genomes (KEGG) pathway analyses, were conducted using the clusterProfiler package in R (v4.5.0)

13. Animals and Tumor Model

All animal experiments were approved by the Institutional Animal Care and Use Committee of Shanghai Jiao Tong University

(Ethical code: A2026094). A subcutaneous prostate tumor model was established by injecting RM1 cells (2×10^6 cells in 100 μL PBS) into the right flank of five-week-old male C57BL/6 mice.

Tumor growth was monitored by measuring the tumor length and width using a digital caliper, and tumor volume (V) was calculated according to the following eq 3:

$$Tumor\ volome(V) = \frac{width^2 \times length}{2} \quad (3)$$

When the tumor volume reached approximately 150 mm^3, the mice were randomly assigned to different groups for subsequent in vivo and ex vivo experiments.

14. PA Imaging

A subcutaneous tumor model was established by inoculating RM1 cells into five-week-old male C57BL/6 mice. After 14 days, when the tumors reached an appropriate size, CuS@Cel/PCM-MPNs were intravenously injected via the tail vein (final Cel dose: 0.5 mg/kg). Photoacoustic (PA) imaging was performed at the tumor site at predetermined time points (0, 2, 6, 12, and 24 h post-injection) using a Vevo LAZR-X multimodal imaging system (FUJIFILM VisualSonics, USA). The excitation wavelength was set in the near-infrared region according to the absorption characteristics of CuS.

15. MRI Imaging

A subcutaneous tumor model was established in five-week-old male C57BL/6 mice by inoculation of RM1 cells. After 14 days of tumor growth, CuS@Cel/PCM-MPNs were intravenously administered via the tail vein (Cel dose: 0.5 mg/kg). Magnetic resonance imaging (MRI) was performed before injection and at 1, 2, and 3 h post-injection using a 9.4 T MRI system (Bruker, Germany). T_1-weighted images were acquired to evaluate the contrast enhancement at the tumor site. The MRI signal intensity at the tumor region was quantitatively analyzed using ImageJ software..

16. Hemolysis Assay

To evaluate the hemocompatibility of CuS@Cel/PCM-MPNs, red blood cells (RBCs) were collected from healthy C57BL/6 mice. Briefly, whole blood was obtained and centrifuged at 3000 rpm for 15 min at 4°C to isolate RBCs, followed by washing three times with PBS. The purified RBCs were then incubated with CuS@Cel/PCM-MPNs dispersed in PBS at different concentrations. PBS and deionized water were used as negative and positive controls, respectively. The mixtures were incubated at 37°C for 2 h and subsequently centrifuged at 3000 rpm for 15 min to collect the supernatants. The absorbance of the supernatants was measured at 492 nm using a microplate reader. The hemolysis ratio was calculated according to the following eq 4:

$$\text{Hemolysisrate}(\%) = \frac{(OD_{Sample} - OD_{Negative\ control})}{(OD_{Positive\ control} - OD_{Negative\ control})} \times 100\% \quad (4)$$

17. In vivo therapeutic efficacy in mouse tumors

Tumor-bearing C57BL/6 mice were randomly divided into five groups (n = 3 per group) and intravenously injected with PBS, CuS, Cel, CuS@Cel, or CuS@Cel/PCM-MPNs (The mice received CuS@Cel/PCM-MPNs at a dose of approximately 8 mg/kg, corresponding to a Cel dose of 0.5 mg/kg and a calculated Cu element dose of approximately 5 mg/kg). At 24 h post-injection, the tumor sites were irradiated with a 1064 nm laser (1.0 W/cm^2) for 5 min. During irradiation, infrared thermal imaging was performed at 2 min intervals to monitor temperature changes at the tumor region. Tumor volume and body weight were recorded every 2 days to evaluate therapeutic efficacy and systemic toxicity. After 12 days of treatment, the mice were sacrificed, and blood samples, tumors, and major organs (heart, liver, spleen, lungs, and kidneys) were collected for further analysis. Immunofluorescence staining of tumor tissues was conducted to analyze the expression of cuproptosis-related proteins, including FDX1 and HSP70. In addition, hematoxylin and eosin (H&E) staining was performed to assess histopathological changes in major organs. Tumor sections were further subjected to Ki-67 staining to evaluate cell proliferation and TUNEL staining to detect apoptosis. In addition,

18. Statistical Analysis

All the results in this study were reported as means ± SD. Statistical significance was evaluated using two-way analysis of variance (ANOVA). The results were deemed statistically significant when $*p < 0.05$, $**p < 0.01$.

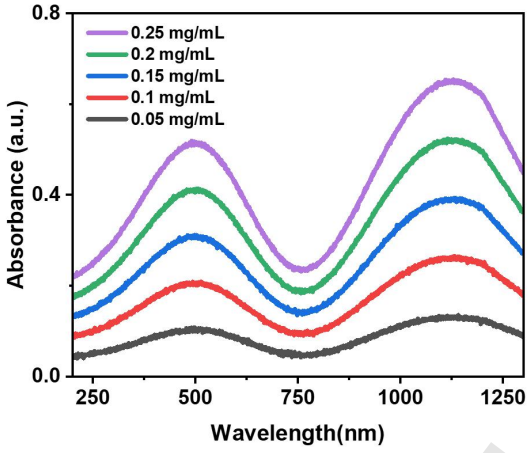

Figure S1. UV-Vis Spectra of CuS at different concentrations.

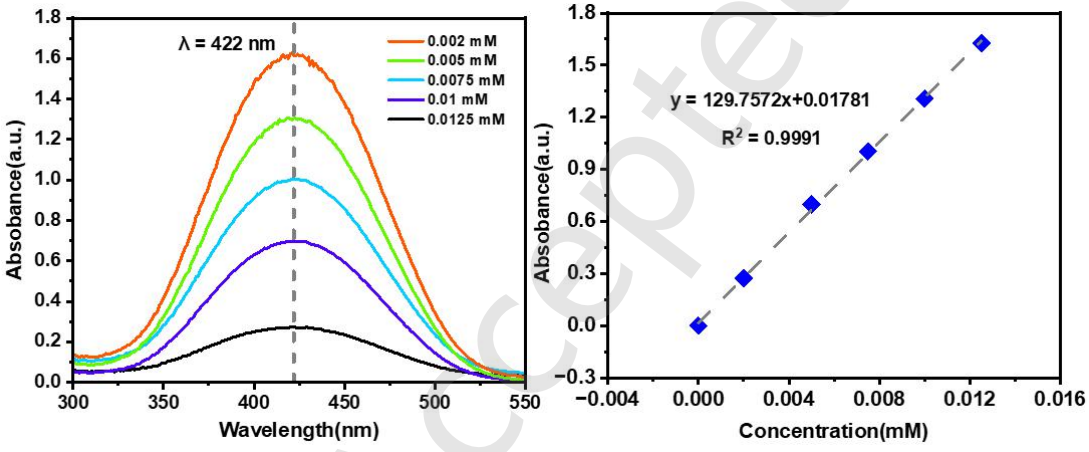

Figure S2. UV-Vis spectra and calibration curves of Cel at different concentrations.

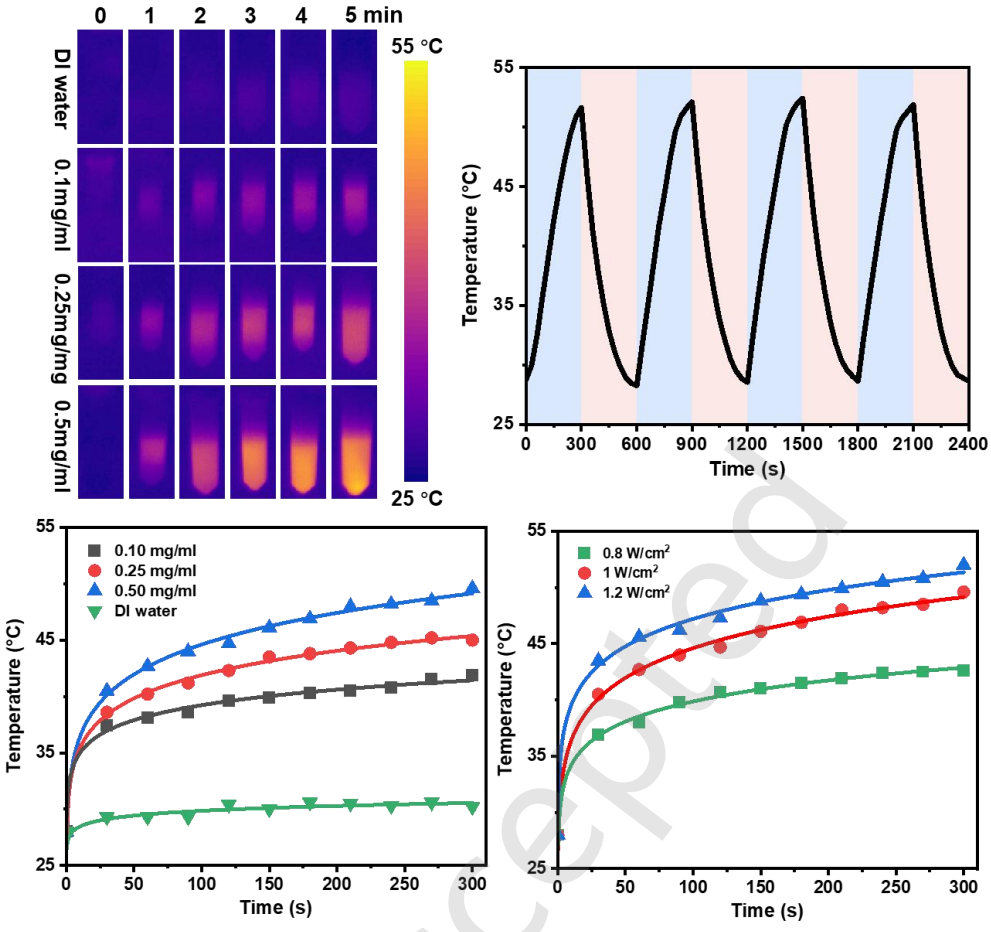

Figure S3. Photothermal properties of CuS.

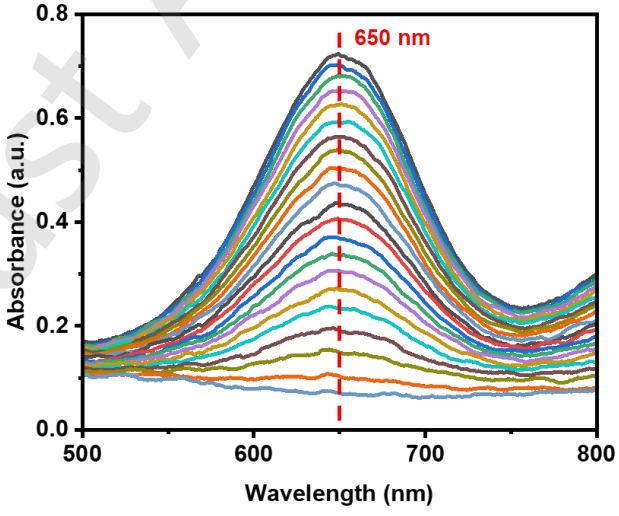

Figure S4. UV-Vis spectra of TMB at different time points.

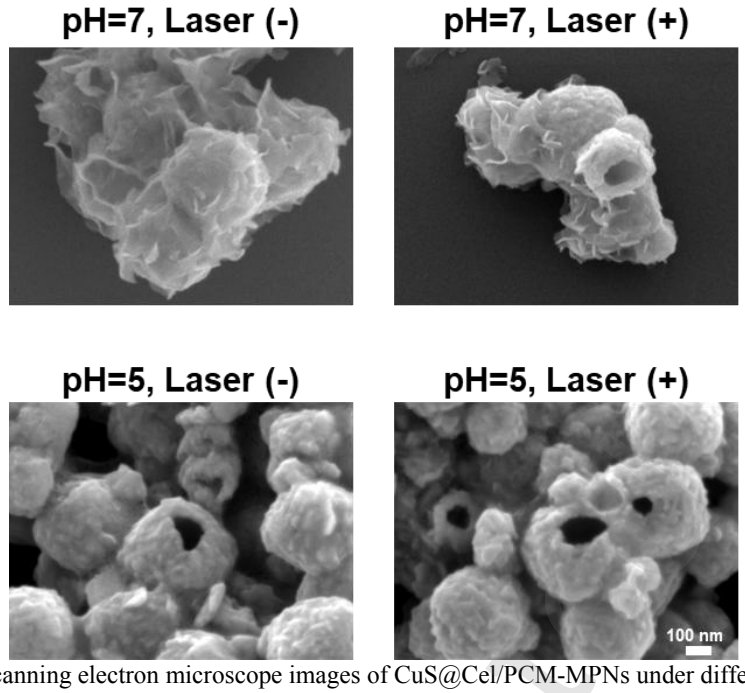

Figure S5. Scanning electron microscope images of CuS@Cel/PCM-MPNs under different conditions.

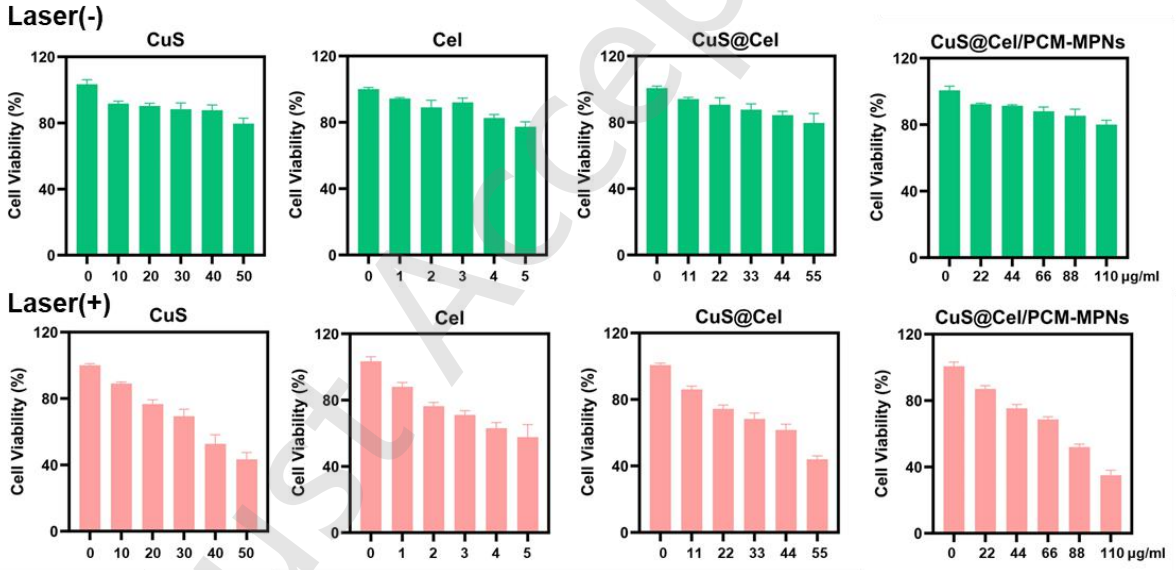

Figure S6. Cell viabilities of RM1 cells incubated with CuS, Cel, CuS@Cel, and CuS@Cel/PCM-MPNs at various concentrations without 1064 nm laser irradiation and under 1064 nm laser irradiation.

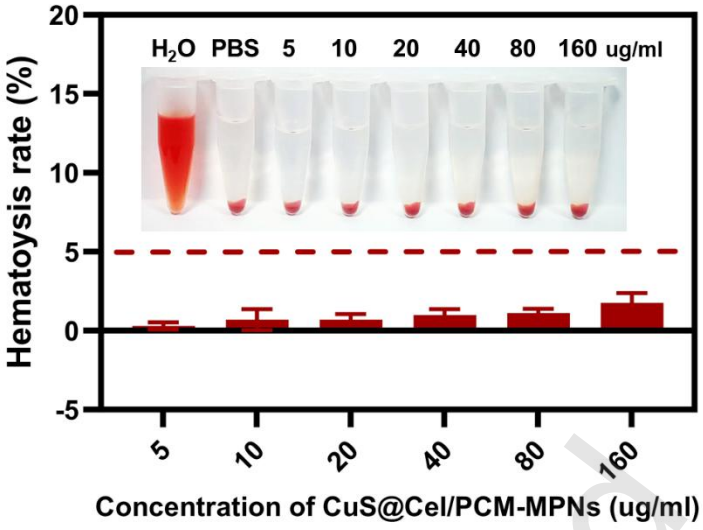

Figure S7. Hematolysis rate of CuS@Cel/PCM-MPNs at different concentrations.

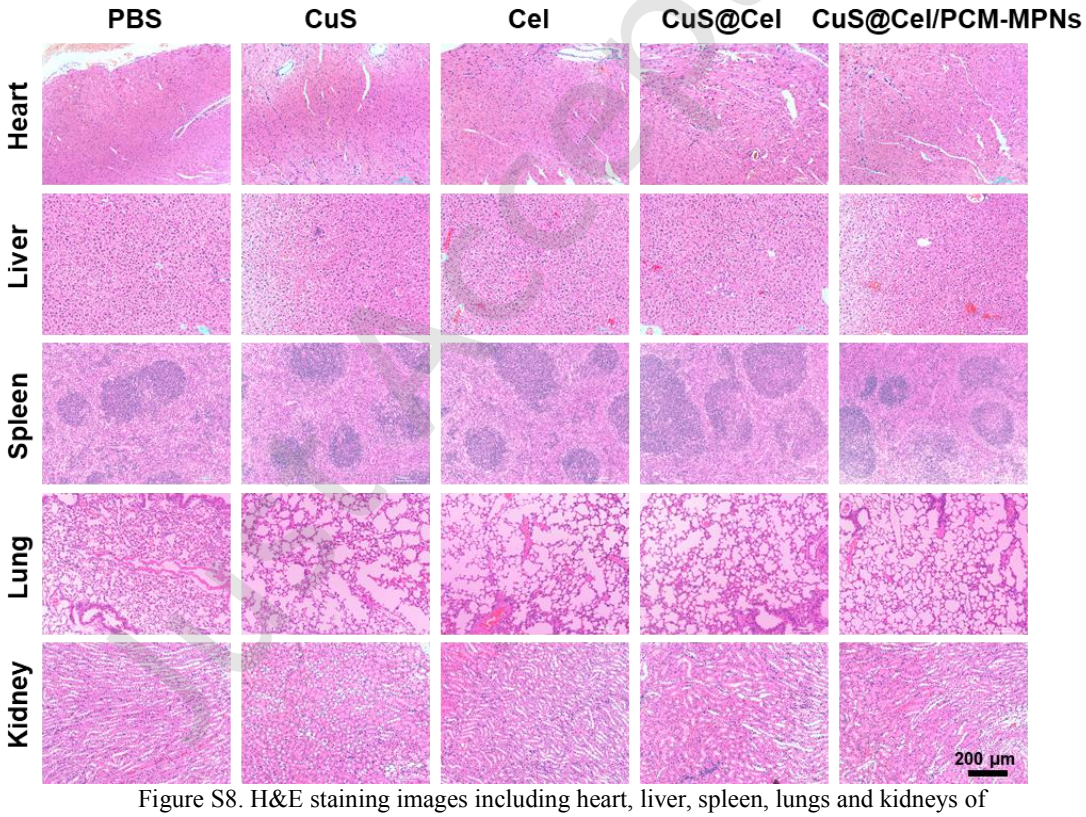

Figure S8. H&E staining images including heart, liver, spleen, lungs and kidneys of mice from different treatment groups.

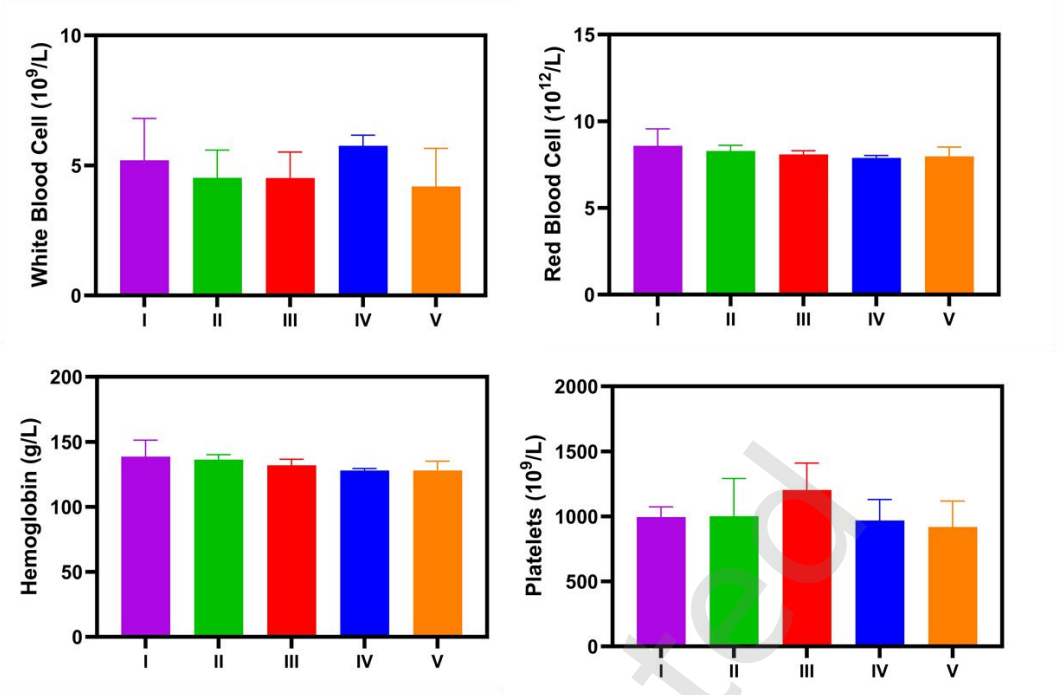

Figure S9. Complete blood count results (Group I: PBS; Group II: CuS; Group III: Cel; Group IV: CuS@Cel; Group V: CuS@Cel/PCM-MPNs).

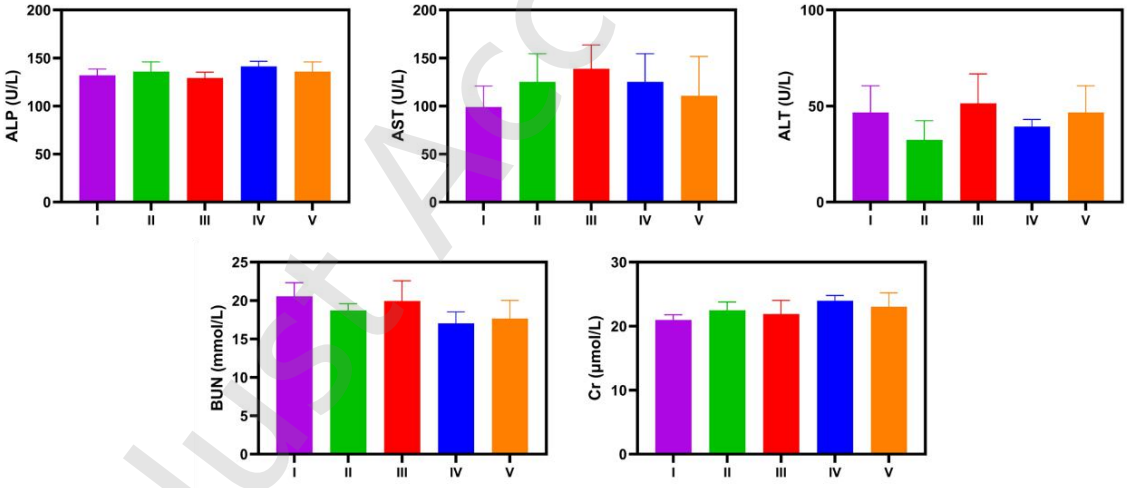

Figure S10. Blood biochemistry results (Group I: PBS; Group II: CuS; Group III: Cel; Group IV: CuS@Cel; Group V: CuS@Cel/PCM-MPNs).